Systems/Circuits

Function and Circuitry of VIP$^+$ Interneurons in the Mouse Retina

Silvia J.H. Park,[1] Bart G. Borghuis,[1,4] Pouyan Rahmani,[1] Qiang Zeng,[1] In-Jung Kim,[1,2]* and Jonathan B. Demb[1,3]*

Departments of [1]Ophthalmology and Visual Science, [2]Neurobiology, and [3]Cellular and Molecular Physiology, Yale University School of Medicine, New Haven, Connecticut 06511, and [4]Department of Anatomical Sciences and Neurobiology, University of Louisville School of Medicine, Louisville, Kentucky 40202

Visual processing in the retina depends on coordinated signaling by interneurons. Photoreceptor signals are relayed to ~20 ganglion cell types through a dozen excitatory bipolar interneurons, each responsive to light increments (ON) or decrements (OFF). ON and OFF bipolar cell pathways become tuned through specific connections with inhibitory interneurons: horizontal and amacrine cells. A major obstacle for understanding retinal circuitry is the unknown function of most of the ~30–40 amacrine cell types, each of which synapses onto a subset of bipolar cell terminals, ganglion cell dendrites, and other amacrine cells. Here, we used a transgenic mouse line in which vasoactive intestinal polypeptide-expressing (VIP$^+$) GABAergic interneurons express Cre recombinase. Targeted whole-cell recordings of fluorescently labeled VIP$^+$ cells revealed three predominant types: wide-field bistratified and narrow-field monostratified cells with somas in the inner nuclear layer (INL) and medium-field monostratified cells with somas in the ganglion cell layer (GCL). Bistratified INL cells integrated excitation and inhibition driven by both ON and OFF pathways with little spatial tuning. Narrow-field INL cells integrated excitation driven by the ON pathway and inhibition driven by both pathways, with pronounced hyperpolarizations at light offset. Monostratified GCL cells integrated excitation and inhibition driven by the ON pathway and showed center-surround spatial tuning. Optogenetic experiments showed that, collectively, VIP$^+$ cells made strong connections with OFF δ, ON-OFF direction-selective, and W3 ganglion cells but weak, inconsistent connections with ON and OFF α cells. Revealing VIP$^+$ cell morphologies, receptive fields and synaptic connections advances our understanding of their role in visual processing.

Key words: **amacrine cell; optogenetics; receptive field; retinal circuitry; transgenic mice; vasoactive intenstinal polypeptide**

Significance Statement

The retina is a model system for understanding nervous system function. At the first stage, rod and cone photoreceptors encode light and communicate with a complex network of interneurons. These interneurons drive the responses of ganglion cells, which form the optic nerve and transmit visual information to the brain. Presently, we lack information about many of the retina's inhibitory amacrine interneurons. In this study, we used genetically modified mice to study the light responses and intercellular connections of specific amacrine cell types. The results show diversity in the shape and function of the studied amacrine cells and elucidate their connections with specific types of ganglion cell. The findings advance our understanding of the cellular basis for retinal function.

Introduction

The retina computes ~20 parallel streams of visual information, conveyed to the brain by as many ganglion cell types (Masland, 2012a; Dunn and Wong, 2014). Each ganglion cell computation depends on specific interneuron elements that form the presynaptic circuit (Seung and Sümbül, 2014). Retinal interneurons comprise three classes (Masland, 2012a,b): bipolar cells (~13 types), narrow-field excitatory interneurons that convey photo-

Received Jan. 16, 2015; revised June 10, 2015; accepted June 15, 2015.

Author contributions: S.J.H.P., B.G.B., I.-J.K., and J.B.D. designed research; S.J.H.P., B.G.B., P.R., Q.Z., and I.-J.K. performed research; S.J.H.P., B.G.B., I.-J.K., and J.B.D. analyzed data; S.J.H.P., B.G.B., I.-J.K., and J.B.D. wrote the paper.

This work was supported by National Institutes of Health Grants R01 EY014454, R21 EY023038, and R00 EY019355, the Whitehall Foundation, the E. Matilda Ziegler Foundation, and a Research to Prevent Blindness unrestricted grant to Yale University. We thank Dr. Joshua Sanes (Harvard University) for kindly providing the CMV-Synaptophysin-YFP construct used in this study and Dr. Steve Massey (University of Texas Medical School at Houston) for technical advice regarding Neurobiotin injection experiments.

B.G.B. owns Borghuis Instruments, which sells the specialized syringe that was used for intravitreal injection in this study. The remaining authors declare no competing financial interests.

*I.-J.K. and J.B.D. contributed equally to this work as co-senior authors.

Correspondence should be addressed to either Dr. In-Jung Kim or Dr. Jonathan B. Demb, 300 George Street, Suite 8100, New Haven, CT 06511, E-mail: in-jung.kim@yale.edu or jonathan.demb@yale.edu.

DOI:10.1523/JNEUROSCI.0222-15.2015

 0270-6474/15/3510685-16$15.00/0

receptor signals to amacrine and ganglion cells (Cohen and Sterling, 1990; Wässle et al., 2009; Helmstaedter et al., 2013; Euler et al., 2014); horizontal cells (one or two types), laterally projecting inhibitory interneurons that make synapses with photoreceptor synaptic terminals and bipolar cell dendrites (Peichl and González-Soriano, 1994; Thoreson and Mangel, 2012); and amacrine cells (~30–40 types), laterally projecting interneurons that make synapses with axon terminals of bipolar cells and the dendritic arbors of ganglion cells and other amacrine cells (Kolb et al., 1981; MacNeil and Masland, 1998; MacNeil et al., 1999). Among the interneuron classes, amacrine cells show the greatest structural diversity, with dendritic/axonal field diameters ranging from extremely narrow (~20 μm) to extremely wide (Völgyi et al., 2001; Badea and Nathans, 2004; Lin and Masland, 2006; Pang et al., 2012) (~2 mm). Amacrine cell synapses primarily inhibit (e.g., via GABA or glycine release) but can also excite (e.g., via acetylcholine or glutamate release) postsynaptic cells (Masland, 2012b; Zhang and McCall, 2012; Lee et al., 2014).

Most ganglion cell computations change dramatically when amacrine cell synapses are blocked, illustrating their fundamental importance in circuit function (Caldwell and Daw, 1978; Caldwell et al., 1978; Roska and Werblin, 2001; Werblin, 2010; Jadzinsky and Baccus, 2013). Direct studies of amacrine cells in mammalian retina have focused primarily on four types, each with a unique function: the AII amacrine cell conveys rod photoreceptor signals to ON and OFF bipolar cell pathways (Kolb, 1979; Demb and Singer, 2012); the A17 amacrine cell generates negative feedback at rod bipolar cell axon terminals (Kolb and Nelson, 1983; Grimes et al., 2010); the starburst amacrine cell generates direction selectivity through GABA release (Euler et al., 2002; Lee and Zhou, 2006; Wei et al., 2011; Vaney et al., 2012); and the dopaminergic amacrine cell drives circadian changes in visual sensitivity throughout the retina (Gustincich et al., 1997; Jackson et al., 2012; Newkirk et al., 2013; McMahon et al., 2014). However, for most other amacrine cell types a basic understanding of receptive field properties and postsynaptic targets is lacking.

To elucidate novel amacrine cell circuits, we used a transgenic mouse line in which VIP$^+$ GABAergic interneurons express Cre recombinase (Taniguchi et al., 2011; Zhu et al., 2014). Targeted electrophysiological recordings and dye filling in the whole-mount retina revealed three distinct VIP$^+$ cell types, each with a unique pattern of dendrite stratification, synaptic input, and receptive field. Optogenetics identified synapses between VIP$^+$ cells and a subset of ganglion cell types, including OFF δ, W3, and ON-OFF direction-selective cells. These studies of VIP$^+$ cell morphologies, receptive fields, and synaptic connections represent an important step in understanding their role in visual processing.

Materials and Methods

Animals. All animal procedures were approved by the Institutional Animal Care and Use Committee at Yale University and were in compliance with National Institutes of Health guidelines. Mice of either sex, maintained on C57BL/6J backgrounds, were studied at ages between 3 weeks and 6 months. In VIP-ires-Cre mice (VIP$^{tm1(cre)Zjh}$/J; The Jackson Laboratory), expression of Cre recombinase is driven by endogenous VIP regulatory elements (Taniguchi et al., 2011). Ai14 mice (B6;129S6-Gt(ROSA)26Sor$^{tm14(CAG-tdTomato)Hze}$/J; The Jackson Laboratory) express a Cre-dependent red fluorescent protein (tdTomato) (Madisen et al., 2010); and Ai32 mice (B6;129S-Gt(ROSA)26Sor$^{tm32(CAG-COP4*H134R/EYFP)Hze}$/J; The Jackson Laboratory) express a Cre-dependent Channelrhodopsin-2 (ChR2)/enhanced yellow fluorescent protein (EYFP) fusion protein (Madisen et al., 2012). TYW3 transgenic mice were generated as described previously (Kim et al., 2010). The TYW3 line labels two types of ganglion cell with green fluorescent protein (GFP): one brightly and the other dimly. Here, we studied the cell type with a small (~10 μm diameter), brightly labeled soma, referred to as W3 cells (Kim et al., 2010; Zhang et al., 2012).

Construction and production of recombinant adeno-associated virus (rAAV). We modified two AAV vectors (Addgene #32481, #32475) to subclone our genes of interest. We cut the DNA of #32481 with NheI and SacI, kept the vector backbone, and ligated it with the insert fragment that was cut out with NheI and SacI from the DNA of #32475. The final product contained NheI and KpnI restriction sites between two nested pairs of incompatible lox sites (pAAV-*hSYN*-Flex-rev-NheI/KpnI-WPRE-pA). We amplified synaptophysin-YFP (SYP-YFP) by PCR, generated NheI and KpnI sites at the end of each sequence, and subcloned PCR products into pAAV-*hSYN*-Flex-rev-NheI/KpnI-WPRE-pA. The plasmid carrying SYP-YFP was kindly provided by Dr. Joshua Sanes (Harvard University).

Virus production was based on a triple-transfection, helper-free method, and virus was purified as described previously (Hommel et al., 2003). Briefly, 10 15-cm plates of HEK293 cells in exponential growth phase were transfected with DNA using polyethylenimine, to increase transfection efficiency; DNA mixtures contained pAAV-RC (carrying replication and capsid 2/1 genes; UPenn Vector Core), pδF6 (carrying adenovirus-derived genes; UPenn Vector Core), and pAAV vector (carrying inverted terminal sequences and the gene of interest). Cells were harvested 48–60 h after transfection. Viral vectors were purified using a step gradient of iodixanol by ultracentrifugation, buffer-exchanged to PBS, and concentrated using Ultracel (Millipore). The rAAV titer was determined by Q-PCR using primers that recognize inverted terminal sequences, and concentrated titers were $>10^{12}$ viral genome particles/ml in all preparations. Viral stocks were stored at −80°C.

One experiment used viral delivery of intensity-based glutamate sensing fluorescent reporter (iGluSnFR) under the control of the human *synapsin*-1 promoter (AAV2/1-*hSYN*-iGluSnFR). This virus was generated in the laboratory of Dr. Loren Looger (Howard Hughes Medical Institute, Janelia Farm), as described previously (Borghuis et al., 2013; Marvin et al., 2013).

Intraocular eye injection. A mouse was anesthetized by intraperitoneal injection of ketamine/xylazine. A small hole was made in the eye with an insect pin to release intraocular pressure. For the SYP-YFP experiment, 0.5–1 μl of rAAV (~10^{12} viral genome particles/ml) was delivered into the vitreous body with a pulled glass micropipette through a small hole in the eye using a pressure injector (Harvard Apparatus). Three to 4 weeks later, mice were anesthetized and perfused transcardially with 4% PFA in 0.1 M phosphate buffer (PB: pH 7.4). For the iGluSnFR experiment, 0.8 μl of rAAV (~10^{13} viral genome particles/ml) was delivered into the vitreous body with a modified Hamilton syringe, as described previously (Borghuis et al., 2013). Three weeks later, the retina was prepared for *in vitro* imaging experiments, as described below.

Electrophysiology. The retina from a mouse between 5 weeks and 6 months of age was prepared as described previously (Borghuis et al., 2013, 2014). Following death, the eye was enucleated and prepared for recording using infrared light and night-vision goggles connected to a dissection microscope. In the recording chamber, a retina was perfused (~4–6 ml/min) with oxygenated (95% O_2–5% CO_2) Ames medium (Sigma-Aldrich) at 32°C–34°C and imaged using a custom-built two-photon fluorescence microscope controlled with ScanImage software (Pologruto et al., 2003; Borghuis et al., 2011, 2013). Fluorescent cells were targeted for whole-cell patch-clamp recording using 910 nm light, as described previously (Park et al., 2014). Membrane current or potential was amplified, sampled at 10 kHz, and stored on a computer (MultiClamp 700B amplifier; Digidata 1440A A-D board; pClamp 10.0 software; Molecular Devices). Patch pipettes (5–11 MΩ) contained the following (in mM): 120 Cs-methanesulfonate, 5 TEA-Cl, 10 HEPES, 10 BAPTA, 3 NaCl, 2 QX-314-Cl, 4 ATP-Mg, 0.4 GTP-Na_2, and 10 phosphocreatine-$Tris_2$ (pH 7.3, 280 mOsm) for voltage-clamp recording; and 120 K-methanesulfonate, 10 HEPES, 0.1 EGTA, 5 NaCl, 4 ATP-Mg, 0.4 GTP-Na_2, and 10 phosphocreatine-$Tris_2$ (pH 7.3, 280 mOsm) for current-clamp recording. Either Lucifer yellow (0.1%) or red fluorophores (sulforhodamine, 10 μM or Alexa-568, 60 μM) were added to the pipette solution for visualizing the cell. All drugs used for electrophysi-

ology experiments were purchased from Tocris Biosciences or Sigma-Aldrich. Excitatory and inhibitory currents were recorded at holding potentials near the estimated reversal for either chloride (E_{Cl}, −67 mV) or cations (E_{cation}, 0 mV), after correcting for the liquid junction potential (−9 mV). Series resistance (~20–70 MΩ) was compensated by 50%. Following the recording, an image of the filled cell was acquired using the two-photon microscope.

Unlabeled ganglion cells were targeted based on soma size: ~15 μm diameter for ON-OFF direction-selective (DS) ganglion cells and ~20–25 μm diameter for OFF δ, OFF α, and ON α cells (Pang et al., 2003; Murphy and Rieke, 2006; Park et al., 2014). In these cases, cell identity was confirmed by the characteristic spike response to light stimuli (loose-patch recording, Ames-filled pipette) and by the dendritic morphology, imaged following the whole-cell recording (Margolis and Detwiler, 2007; Borghuis et al., 2014). Furthermore, ON α cell identity was confirmed by measuring a slow melanopsin-mediated excitatory current in response to a bright blue ChR2-activating stimulus in the presence of synaptic blockers (Estevez et al., 2012; Beier et al., 2013) (see Results).

Stimuli were presented using a modified video projector (peak output, 395 nm) (Borghuis et al., 2013, 2014) focused onto the retina through the microscope condenser. The stimulus wavelength about equally effectively stimulates cone photoreceptors along the retina's dorsal/ventral gradient (Borghuis et al., 2014), which coexpress varying ratios of middle (M) and short-wavelength (S) sensitive opsins (Applebury et al., 2000; Nikonov et al., 2006; Wang et al., 2011; Baden et al., 2013). Stimuli were presented within a 4 × 3 mm area on the retina. Stimuli included contrast-reversing spots of variable diameter, to measure spatial tuning (Zhang et al., 2012), and drifting gratings, to measure direction selectivity (Park et al., 2014). Spot stimuli were presented with 1 Hz temporal square-wave modulations (100% Michelson contrast) relative to a background of mean luminance that evoked ~10^4 photoisomerizations (R*) cone^{-1} sec^{-1} (Borghuis et al., 2014).

For some experiments, the synaptic response was recorded at a series of holding potentials (V_{holds}) using the Cs-based solution described above. The excitatory (or inhibitory) current was calculated as a weighted average of the response at the two V_{holds} on either side of the calculated inhibitory (or excitatory) reversal potential (i.e., weighted inversely by the difference between each V_{hold} and the reversal potential). Input resistance was calculated using the Membrane Test function in pClamp software (20 mV step).

Neurobiotin injection. A sharp pipette (~400 MΩ resistance) filled with Lucifer yellow (0.2%) and Neurobiotin (4%; Vector Laboratories) in 0.1 M Tris-buffered saline was advanced to impale a fluorescent VIP$^+$ cell. Negative current was used briefly to inject Lucifer yellow and confirm the injected cell's identity. Subsequently, positive current was used to inject Neurobiotin into the cell (1 nA, ~15 min). The tissue was then fixed, and filled cells were visualized by reacting for 2 h with streptavidin-AlexaFluor-647 (1:200, Jackson ImmunoResearch Laboratories). Images were analyzed by confocal microscopy, using methods described below. We analyzed coupled Neurobiotin$^+$ somas that were >30 μm from the injected bistratified inner nuclear layer (INL) cell body, to avoid cells labeled by possible leakage of the tracer near the injection site.

Histology. For immunohistochemistry, the animal was perfused at ages 3–5 weeks. The retinas were dissected and fixed with 4% PFA for 1 h at 4°C. For whole-mount staining, retinas were incubated with 2%–3% donkey serum/0.2%-0.3% Triton X-100/TBS for 1 h at room temperature, with primary antibodies for 1–4 d at 4°C, and with secondary antibodies for 1–2 h at room temperature. For the cryosections, retinas were incubated in 30% sucrose/PBS for 2 h after fixation, frozen, and sectioned at 18–25 μm. For morphological analysis of recorded cells, the retina was fixed for 1 h at room temperature and reacted as described previously (Manookin et al., 2008).

Primary antibodies were used at the following concentrations: chicken anti-GFP (1:1000, Aves Laboratories), rabbit anti-GFP (1:1000, Millipore), rabbit anti-VIP (1:500, Immunostar), goat anti-ChAT (1:250, Millipore), rabbit anti-DsRed (1:1000, Clontech), rabbit anti-TH (1:1000, Millipore), rabbit anti-GAD65/67 (1:1000, Millipore), rabbit anti-GlyT1 (1:1000, Millipore), rabbit anti-Lucifer yellow (1:2000, Invitrogen), and mouse anti-CD15 (1:50, DSHB). Secondary antibodies were conjugated to AlexaFluor-488, Cy3 and Cy5 (Jackson Immuno Research Laboratories) and diluted at 1:200 or 1:500.

Dendritic tree size and stratification analysis. Confocal imaging was performed using a Zeiss LSM 5 Exciter confocal microscope. A whole-mount image of the entire dendritic tree was acquired using either a 20× air objective (NA = 0.8) or a 40× oil objective (NA = 1.4); in some cases, multiple images were combined as a montage to capture the entire tree. The dendritic tree diameter was determined using National Institutes of Health ImageJ by drawing a convex polygon that included all dendrites, and measuring the area. Below, we report the diameter of a circle with an area equivalent to the polygon. A high-resolution *z*-stack of the ChAT bands (i.e., cholinergic starburst amacrine cell processes, labeled by the ChAT antibody) and the filled VIP$^+$ cell was obtained to determine their relative depth in the IPL. In addition, we confirmed that each filled cell was labeled with either tdTomato (VIP-ires-Cre::Ai14 mice) or EYFP (VIP-ires-Cre::Ai32 mice).

Custom software written in MATLAB (The MathWorks) was used to determine VIP$^+$ cell dendrite stratification relative to the ChAT bands. The program and methods used were similar to those described previously (Manookin et al., 2008; Farrow et al., 2013; Sümbül et al., 2014). Labeled VIP$^+$ cell dendrites and the ChAT bands were imaged using the 40× objective. Each frame of the *z*-stack was 160 × 160 μm (512 × 512 or 1024 × 1024 pixels) with either 0.5 or 1.0 μm spacing in the *z* dimension. Each frame was divided into 16 (4 × 4) square 40 × 40 μm regions. For ~4 of these regions, the fluorescence peaks of the ChAT bands, in the *z* dimension, were fit (polynomial functions) and aligned to 0 (peak of inner ChAT band) and 1 (peak of outer ChAT band) in normalized units. Normalized data from each region were then averaged, and the peak VIP$^+$ amacrine cell fluorescence signal was fit, as described above.

Data are reported as mean ± SEM unless indicated otherwise. In those cases where we tested a specific hypothesis, statistical comparison was made with a one-tailed *t* test, as follows. We predicted that: (1) inhibitory receptor antagonists would block inhibitory currents; (2) L-AP4 would block ON responses; and (3) ChR2 would evoke an increase in inhibitory synaptic conductance in postsynaptic ganglion cells. In all other cases, there was not a specific hypothesis, and statistical comparison was based on a two-tailed *t* test.

Results

In the experiments described below, we aimed to do the following: (1) distinguish and identify the primary types of VIP$^+$ amacrine cell types in the mouse retina; (2) determine the light-evoked synaptic inputs to each cell type; (3) determine the spatial receptive field properties of each cell type; and (4) identify synaptic connections between VIP$^+$ cells and identified ganglion cell types. A recent study, using a viral labeling method different from ours, identified a single type of VIP$^+$ cell with a wide-field, bistratified dendritic tree (Zhu et al., 2014). Our study identified the same type as well as two additional types. The experiments below are, to our knowledge, the first to measure physiological properties and synaptic connections of VIP$^+$ cells.

Characterization of VIP$^+$ cells in transgenic mice

The retina of a VIP-ires-Cre::Ai14 mouse (i.e., offspring of VIP-ires-Cre × Ai14 mice) showed sparse, red fluorescent cells in both the INL and the ganglion cell layer (GCL), as described for a different reporter line (Ai9; Zhu et al., 2014). Most fluorescent somas (87.1%; $n = 310$ cells in 2 animals) were also clearly labeled by a VIP antibody (Fig. 1*A*), suggesting that most tdTomato-expressing cells actively expressed VIP at the time of tissue fixation (3–5 weeks postnatal). VIP$^+$ somas showed no overlap with starburst amacrine somas, labeled with a ChAT antibody (Fig. 1*B*). Relative to the two bands of starburst processes (ChAT bands; see Materials and Methods), VIP$^+$ cell processes concentrated at three levels in the inner plexiform layer (IPL): adjacent

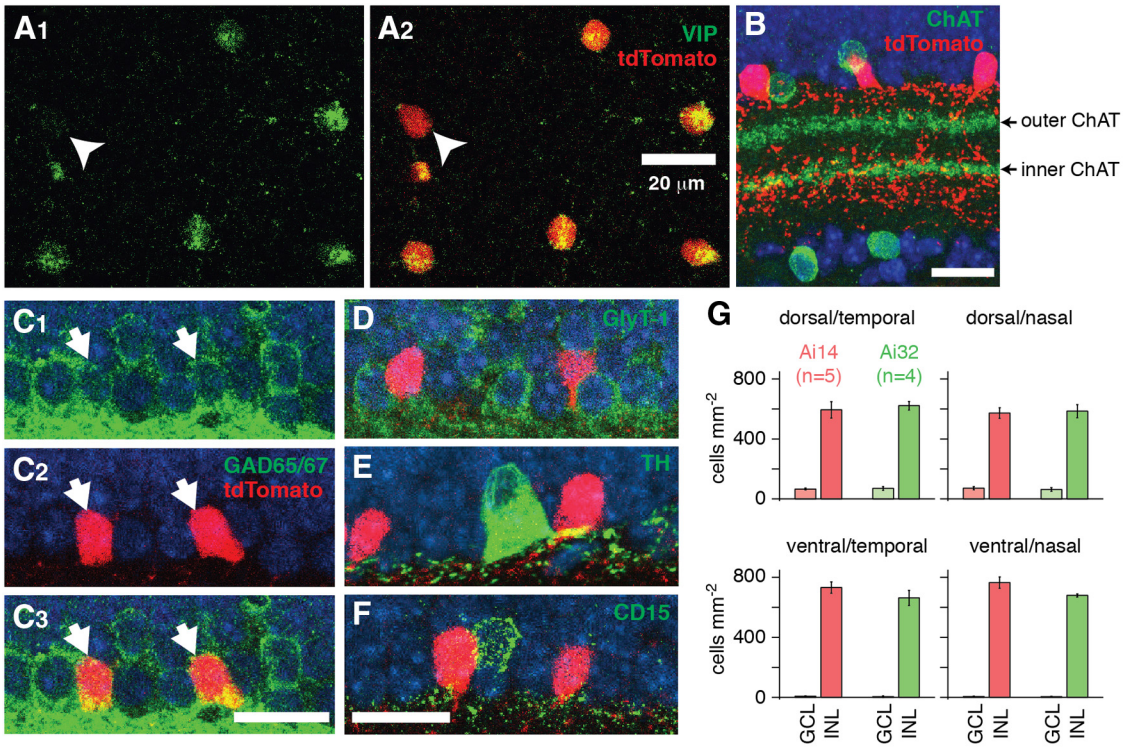

Figure 1. Expression pattern and regional density of VIP+ amacrine cells. ***A***, Confocal fluorescence images of retinal sections. VIP antibody staining (green; A_1) in a VIP-ires-Cre::Ai14 retina overlaps with red fluorescence in most cells (A_2). A rare red cell lacking obvious antibody labeling is shown (arrowhead). All panels: scale bar, 20 μm. ***B***, VIP+ cells (red) stratify in several layers relative to the cholinergic starburst amacrine cells, labeled with a ChAT antibody (green). Inner and outer ChAT bands are indicated. ***C***, Labeling of GAD65/67 antibody (green; C_1) includes VIP+ cells (red; arrowheads in C_2) in a VIP-ires-Cre::Ai14 retina. Overlap is shown in C_3. ***D–F***, VIP+ cells (red) lack staining by antibodies against GlyT1 (green, ***D***), tyrosine hydroxylase (TH; green, ***E***), or CD15 (green, ***F***). All sections show the INL. ***G***, Cell counts from four quadrants (0.32 × 0.32 mm^2 in-plane resolution), 0.5–1.0 mm from the optic disk. *n* indicates the number of retinas used for each cell count with both the Ai14 and Ai32 reporter lines. Error bars indicate ± 1 SEM across retinas.

to the INL, surrounding the inner ChAT band, and between the inner ChAT band and the GCL (Fig. 1*B*) (Lorén et al., 1980; Tornqvist et al., 1982; Sagar, 1987). VIP+ cells were also labeled by an antibody against the GABA precursor, glutamic acid decarboxylase 65/67 (GAD 65/67) (Fig. 1*C*), but not by an antibody against the glycine transporter GlyT1 (Fig. 1*D*) (Casini and Brecha, 1992; Lee et al., 2002). VIP+ cells were not labeled by antibodies against the dopamine precursor tyrosine hydroxylase (n = 25 cells, 2 animals), and there was only minimal overlap with a CD15 antibody (three CD15+ cells among 83 VIP+ cells, 2 animals), which labels two populations of amacrine cell in the mouse retina (Jakobs et al., 2003) (Fig. 1*E*,*F*). These data show that labeled cells in the VIP-ires-Cre::Ai14 retina are GABAergic and predominantly VIP+ (Zhu et al., 2014).

The density of fluorescent cell bodies in the GCL varied across the retina. Somas in the GCL localized primarily to the dorsal retina (Fig. 1*G*). A similar pattern was obtained using a second reporter line (VIP-ires-Cre::Ai32; Fig. 1*G*), with Cre-dependent ChR2/EYFP expression, ruling out an aberrant reporter-specific expression pattern. The total density of fluorescent cells combined across quadrants was similar for the Ai14 (704 ± 107 cells mm^{-2}; mean ± SD; 20 regions, 5 retinas) and Ai32 reporter lines (673 ± 70 cells mm^{-2}; 16 regions, 4 retinas). Averaging across reporter lines, the density of cells in the GCL was higher in the dorsal retina (68 ± 20 cells mm^{-2}) compared with the ventral retina (6 ± 6 cells mm^{-2}; t = 12.6; $p < 0.0001$). Within the dorsal retina, most fluorescent cells were INL cells; GCL cells comprised just 10 ± 3% of the population.

Dendritic morphology of VIP+ cells

An individual VIP+ cell dendritic tree was labeled either through viral delivery of Cre-dependent synaptophysin-YFP (SYP-YFP; n = 34 cells, 4 retinas) or through dye filling following patch-clamp recording (n = 45 cells, 37 retinas; see Materials and Methods). Using either method, we measured dendritic tree area and the stratification level of the dendrites relative to the ChAT bands (Fig. 2). Some VIP+ cells with somas in the INL showed bistratified dendritic trees and occasional long processes or "tails" that extended >100 μm from the primary dendritic tree (Fig. 2*A*,*B*,*H*). This group resembled the VIP+ cells described earlier (Zhu et al., 2014). In addition, a second group of cells in the INL had narrower, monostratified dendritic trees (Fig. 2*C*,*D*,*I*). A third group of cells with somas in the GCL had medium-field, monostratified dendritic trees (Fig. 2*E*,*I*). We occasionally observed cells bearing axon-like processes extending >0.5 mm from the cell body (Fig. 2*F*). These cells were rare and were omitted from further study. For the remaining cell types, data from the dye filling and viral labeling methods were similar and are combined in the analyses below.

We quantified dendrite stratification by measuring each cell's fluorescence-depth profile relative to the fluorescence peaks of the inner and outer ChAT bands, normalized to 0 and 1, respectively (Fig. 2*G*; see Materials and Methods) (Manookin et al., 2008; Sümbül et al., 2014). VIP+ cells were first divided into bistratified and monostratified groups. Bistratified cells showed peak stratification in two regions bracketing the ChAT bands (Fig. 2*H*): adjacent to the INL (1.59 ± 0.12 units; mean ± SD; n = 45 cells) and between the inner ChAT band and the GCL

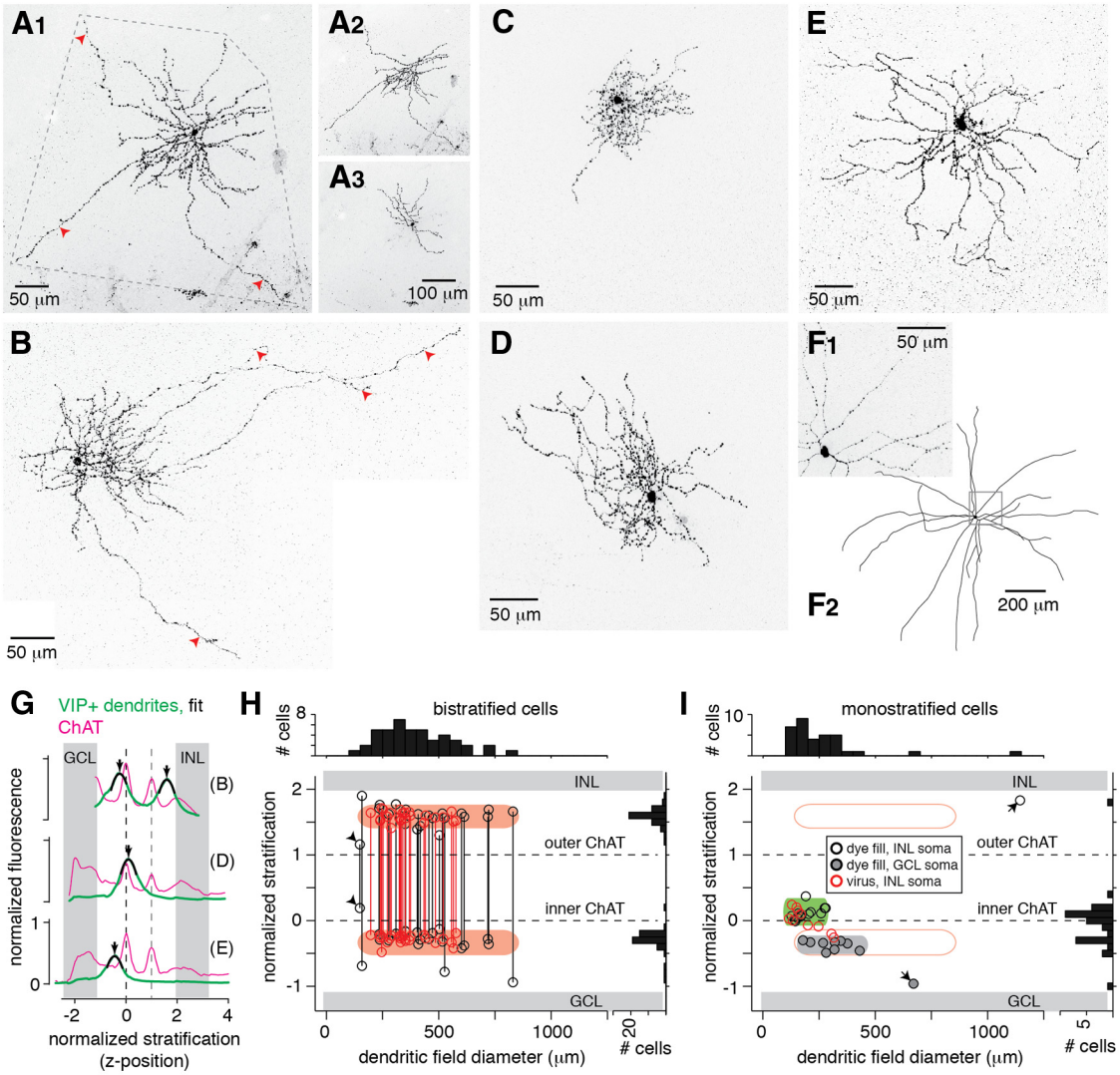

Figure 2. Single-cell morphology reveals distinct types of VIP$^+$ cell. ***A***, *Z*-projection of confocal images of a dye-filled (Lucifer yellow) bistratified INL cell (***A*$_1$**; fluorescence inverted and converted to grayscale). Dendritic tree area is measured with a convex polygon (dashed line). Images represent two dendritic tiers, near the GCL (inner dendrites, ***A*$_2$**) and the INL (outer dendrites, ***A*$_3$**), respectively, with several long "tails" that emerge from the dense arborizations surrounding the cell body (red arrowheads, here and in ***B***). ***B***, A second bistratified INL cell labeled following viral delivery of Synaptophysin-YFP. ***C***, ***D***, Two narrow-field cells (dye-filled). ***E***, A ganglion cell-layer cell (dye-filled). ***F***, Image near the soma of an axon-bearing cell (***F*$_1$**; dye-filled) and a drawing of the entire field of processes (***F*$_2$**). ***G***, Fluorescence profile of a VIP$^+$ cell (green) is shown relative to the ChAT bands (magenta) and the approximate locations of the ganglion cell and inner nuclear layers (GCL, INL; shaded regions) (Tikidji-Hamburyan et al., 2015). ChAT band centers were normalized to 0 (inner band) and 1 (outer band). Arrows indicate peak fluorescence of the VIP$^+$ dendrites (black). The three examples (cells shown in ***B***, ***D***, ***E***) represent cells in each group. ***H***, Scatter plot of dendritic field diameter versus normalized stratification for bistratified cells. Each cell was labeled by either dye fill (black) or viral transduction (red). The two peaks from a single cell are connected. Shaded regions represent areas in the two-dimensional space that include most cells. All cells but one bracket the ChAT bands. The one outlier (arrowheads) had an inner tier of dendrites between the ChAT bands. Histograms represent collapsed data along the two dimensions. ***I***, Same format as ***H*** for monostratified cells. A narrow-field group (green shaded region) primarily stratified between the ChAT bands and adjacent to the inner ChAT band, whereas a second group (gray shaded region) stratified between the inner ChAT band and the GCL. Cells whose soma was in the GCL are represented by gray-filled circles. Two cells filled by virus labeling, but with somas in the INL, seemed to cluster with the GCL cells. The two multiaxonal cells were distinct from the narrow-field and GCL cell distributions (arrows; open circle is the cell in ***F***). Orange outlines represent the positions of bistratified cell dendrites shown in ***H***.

(−0.30 ± 0.17 units). Their dendritic tree diameter was 399 ± 154 μm (range, 150–830 μm; Fig. 2*H*), which included the influence of the few processes extending hundreds of micrometers beyond the primary dendritic field (Fig. 2*A*,*B*).

Most monostratified cells stratified between −0.5 and 0.4 normalized depth units. A dividing point at ~−0.15 units (Fig. 2*I*) was used as a boundary between two cell groups. The first group, narrow-field INL cells, had somas in the INL, showed peak stratification between the ChAT bands, at 0.10 ± 0.11 units (mean ± SD; $n = 21$) (Fig. 2*I*), with processes extending to the inner ChAT band in each case. Their dendritic trees had a diameter of 180 ± 50 μm (range, 115–280 μm; Fig. 2*I*). The second group, monostratified GCL cells, had somas in the GCL, peak stratification between the GCL and the inner ChAT band (−0.37 ± 0.07 units; $n = 9$), and medium-field diameters of 303 ± 79 μm (range, 180–430 μm; Fig. 2*I*). Data from rare multiaxonal cells were clearly distinct from the other cell groups. One cell stratified near the GCL, and the other stratified near the INL; in each case, the soma was positioned in the layer adjacent to its dendrite stratification (Fig. 2*I*).

Overall, the pattern of dendrite stratification across cells suggested three predominant VIP$^+$ cell types: a wide-field bistratified cell with a soma in the INL (bistratified INL cells); a narrow-field cell with a soma in the INL (narrow-field INL cells);

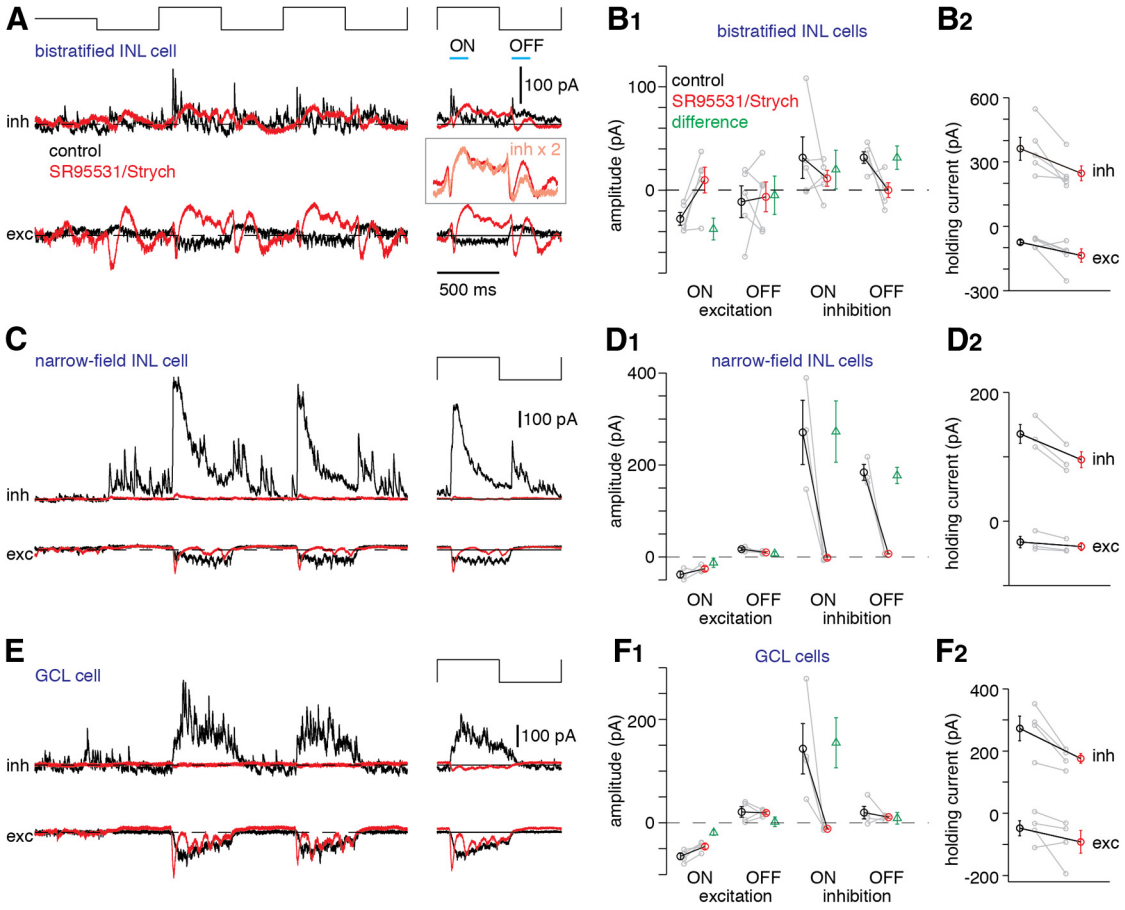

Figure 3. Patterns of synaptic excitation and inhibition in VIP$^+$ cells. ***A***, Left, Voltage-clamp recordings of excitatory current (exc; V_{hold} near inhibitory reversal, −67 mV) and inhibitory current (inh; V_{hold} near excitatory reversal, 0 mV) in a bistratified INL cell in response to a 1 Hz contrast-reversing spot (200 μm diameter, 100% contrast). Red traces represent the same measurements in the presence of antagonists to GABA-A (SR95531, 50 μM) and glycine receptors (strychnine, 1 μM). Traces have been baseline-subtracted. Horizontal dashed line indicates baseline (i.e., average current before the stimulus). Right, Average cycle of excitatory and inhibitory current, combined across two repeats at each of two holding potentials bracketing the appropriate reversal potential (see Materials and Methods). ON and OFF time windows (100–250 ms following either light onset or offset) indicate periods where current was averaged for population analysis (see ***B*$_1$**). Inset, Average excitatory current (red) superimposed on the average inhibitory current scaled by a factor of 2 (orange; inh × 2). In the presence of drugs, the presumed inhibitory current resembled the excitatory current, and apparently reflects unclamped input through an electrical synapse (see Results). ***B*$_1$**, Excitatory and inhibitory input in the ON and OFF time windows in ***A*** in control (black) and drug (red) conditions. Measurements from individual cells are shown in gray. Green points indicate the difference between control and drug conditions. Error bars indicate ±1 SEM across cells. Across cells, spot diameter was either 200 or 300 μm. ***B*$_2$**, The holding current during measurements of excitatory and inhibitory current. Error bars indicate ±1 SEM across cells. ***C***, ***D***, Same format as ***A*** and ***B***, but for narrow-field INL cells. ***E***, ***F***, Same format as ***A*** and ***B***, but for GCL cells.

and a monostratified cell with a soma in the GCL (GCL cells). In a subset of dye-filled cells, we determined the eccentricity of each cell (distance from the optic disk) and distinguished dorsal versus ventral locations. We found no significant correlation between dendritic tree diameter and eccentricity for any of the cell types: bistratified INL cells ($r = 0.03$; $n = 21$); narrow-field INL cells ($r = 0.08$; $n = 13$); and GCL cells ($r = 0.15$; $n = 9$). Furthermore, we did not find different diameters between bistratified INL cells in the dorsal (456 ± 55 μm; $n = 14$) and ventral retina (412 ± 66 μm; $n = 6$) or between narrow-field INL cells in the dorsal (206 ± 25 μm; $n = 6$) and ventral retina (191 ± 20 μm; $n = 5$). (There were too few GCL cells in the ventral retina to compare with cells in the dorsal retina.) In summary, we found no consistent regional variation in VIP$^+$ dendritic tree size for any of the VIP$^+$ cell types.

The three primary VIP$^+$ cell types have distinct patterns of excitatory and inhibitory synaptic input

Synaptic inputs to VIP$^+$ cells were studied by targeted whole-cell patch-clamp recordings in the whole-mount retina ($n = 107$ cells). Each cell was positively identified as one of the three primary cell types described above, based on two-photon imaging of the dendritic tree and/or subsequent analysis by confocal microscopy.

Excitatory and inhibitory synaptic currents were studied by clamping voltage near the appropriate reversal potential (see Materials and Methods). Cone-mediated responses were recorded to spots (200–300 μm diameter) with 100% contrast modulation at 1 Hz (see Materials and Methods; Fig. 3). The bistratified INL cells ($n = 5$) showed sustained excitatory input at light onset with variable degrees of sluggish excitatory input at light offset. Inhibitory input was relatively small, transient, and typically occurred at both light onset and offset (Fig. 3*A*). To assess the quality of the voltage clamp, we tested whether inhibition, measured at the excitatory reversal potential, was eliminated by antagonists to GABA-A receptors (50 μM SR95531) and glycine receptors (1 μM strychnine). The inhibitory receptor antagonists dramatically changed the bistratified INL cell response and, unlike the other two cell types described below, did not null the response at the excitatory reversal potential. Rather, there was an oscillatory response that resembled the excitatory input recorded at the inhibitory reversal but with reduced amplitude (Fig. 3*A*, inset, B_1). The

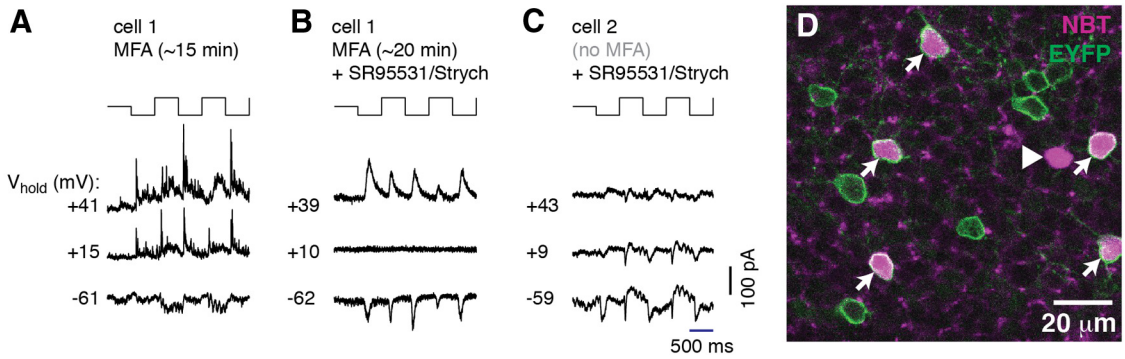

Figure 4. Bistratified INL cells electrically couple to VIP$^+$ cells. ***A***, Voltage-clamp recordings of a bistratified INL cell at three holding potentials. The gap junction blocker MFA had been applied for 15 min at the time of recording. ***B***, Same cell as in ***A*** after adding the inhibitory receptor antagonists SR95531 and strychnine (as in Fig. 3). The gap junction blocker MFA had been applied for 20 min at the time of recording. The response near the excitatory reversal potential ($V_{hold} = 10$ mV) is nulled under these conditions, and the response near the inhibitory reversal potential ($V_{hold} = -62$ mV) is inverted at the positive holding potential ($V_{hold} = 39$ mV). ***C***, Same as in ***B***, but for a cell recorded in the inhibitory blockers without MFA (same cell as in Fig. 3*A*). The response does not reverse. ***D***, Neurobiotin labeling following the injection of a bistratified INL VIP$^+$ cell in a VIP-ires-Cre::Ai32 retina. Most somas labeled by Neurobiotin (NBT; magenta) had their membrane labeled by EYFP (arrows); one cell was Neurobiotin$^+$ only (arrowhead). The image is from a single confocal section centered ~150 μm from the soma of the injected bistratified INL cell.

presumed inhibitory input at light offset (OFF time window) was suppressed by the blockers (by 31 ± 11 pA; $t = 2.8$; $p < 0.05$), whereas the presumed inhibitory input at light onset (ON time window) was not (20 ± 19 pA), reflecting the response variability across cells (Fig. 3B_1). In general, the pattern of results in bistratified INL cells differed from the other two cell types described below and suggested input from electrically coupled cells whose influence increased when inhibitory receptors were blocked, and could not be adequately voltage clamped. A similar inability to voltage clamp was observed in another electrically coupled amacrine cell, the AII (Pang et al., 2007; Ke et al., 2014).

The narrow-field INL cells ($n = 3$) showed sustained excitatory input at light onset, with inhibitory input at both light onset and offset. The inhibitory inputs were notably large and transient (Fig. 3*C*). Pharmacological block of GABA-A and glycine receptors completely suppressed inhibitory input measured in both ON (by 272 ± 67 pA; $t = 4.08$; $p < 0.05$) and OFF time windows (by 177 ± 18 pA; $t = 10.1$; $p < 0.01$) (Fig. 3C,D_1). The ability to record a nulled response at the excitatory reversal potential, with inhibition blocked, suggests that narrow-field INL cells could be adequately voltage clamped and that electrical coupling is absent or weak. Furthermore, the blockers caused the sustained excitatory input to become transient in each cell, followed by small oscillations (Fig. 3*C*).

GCL cells ($n = 4$) showed a third pattern of synaptic input. These cells received coincident sustained excitatory and inhibitory inputs at light onset (Fig. 3*E*). Pharmacological block of GABA-A and glycine receptors suppressed inhibitory input in the ON-time window by 155 ± 49 pA (mean ± SEM; $t = 3.19$; $p < 0.05$), and the response modulation at the excitatory reversal potential was nearly abolished (Fig. 3E,F_1). Thus, GCL cells could be adequately voltage clamped, and electrical coupling is apparently absent or weak. Furthermore, similar to narrow-field INL cells, the blockers caused the sustained excitatory input in GCL cells to become transient in each case, followed by small oscillations (Fig. 3*E*).

In addition to affecting the evoked response, the inhibitory receptor antagonists changed the holding currents (Fig. 3B_2,D_2,F_2). While recording inhibition, the holding current for bistratified INL cells, narrow-field INL cells, and GCL cells was reduced by 114 ± 34 pA ($t = 3.36$; $p < 0.05$), 40.1 ± 2.5 pA ($t = 16.2$, $p < 0.01$), and 96 ± 25 pA ($t = 3.80$; $p < 0.05$), respectively. This pattern of results is consistent with reduced tonic inhibition in the presence of the drugs. The initial holding currents while recording excitation were not significantly changed by the drugs, but in each case the holding current tended to become more negative (Fig. 3B_2,D_2,F_2).

Bistratified INL cells are electrically coupled to both VIP$^+$ and VIP$^-$ cells

The bistratified INL cell type's persistent response at the excitatory reversal potential, with inhibition blocked, suggested electrical coupling (Fig. 3A,B_1). To further test this hypothesis, we repeated the voltage-clamp measurements in the presence of the gap junction blocker meclofenamic acid (MFA, 100 μM) (Pan et al., 2007; Manookin et al., 2008; Veruki and Hartveit, 2009). At this concentration, MFA blocks gap junctions in ~20 min (Veruki and Hartveit, 2009). We recorded a control response ~15 min after applying MFA to the bath and then added the inhibitory blockers (SR95531, strychnine), as above. In the presence of the inhibitory blockers (~20 min after adding the MFA), we recorded a completely nulled response at holding potentials between 0 and 10 mV (Fig. 4A,B; $n = 4$ cells). Thus, the inability to record a nulled response in the absence of MFA (Figs. 3A,B_1, 4*C*) is apparently explained by electrical coupling of bistratified INL cells.

To determine which cells are coupled to bistratified INL cells, we injected them with Neurobiotin in a VIP-ires-Cre::Ai32 retina ($n = 5$ cells). Neurobiotin spread to multiple cell bodies in the INL (Fig. 4*D*), and 80% of these coupled cells (59 of 74 coupled cells, four injections) were also EYFP$^+$, indicating that they were VIP$^+$ cells (Fig. 4*D*). From the anatomical data, we cannot determine whether the coupled VIP$^+$ cells were exclusively bistratified INL cells, as opposed to narrow-field INL cells. However, the lack of apparent coupling in the physiological recordings of narrow-field INL cells (Fig. 3C,D) suggests that bistratified INL cells likely couple primarily to other cells of the same type (i.e., homotypic coupling).

The three primary VIP$^+$ cell types receive distinct patterns of synaptic input mediated by ON and OFF bipolar cells

We next assessed how ON and OFF bipolar cell-mediated synaptic inputs are integrated by the three VIP$^+$ cell types. Synaptic currents were measured before and after blocking ON bipolar cell

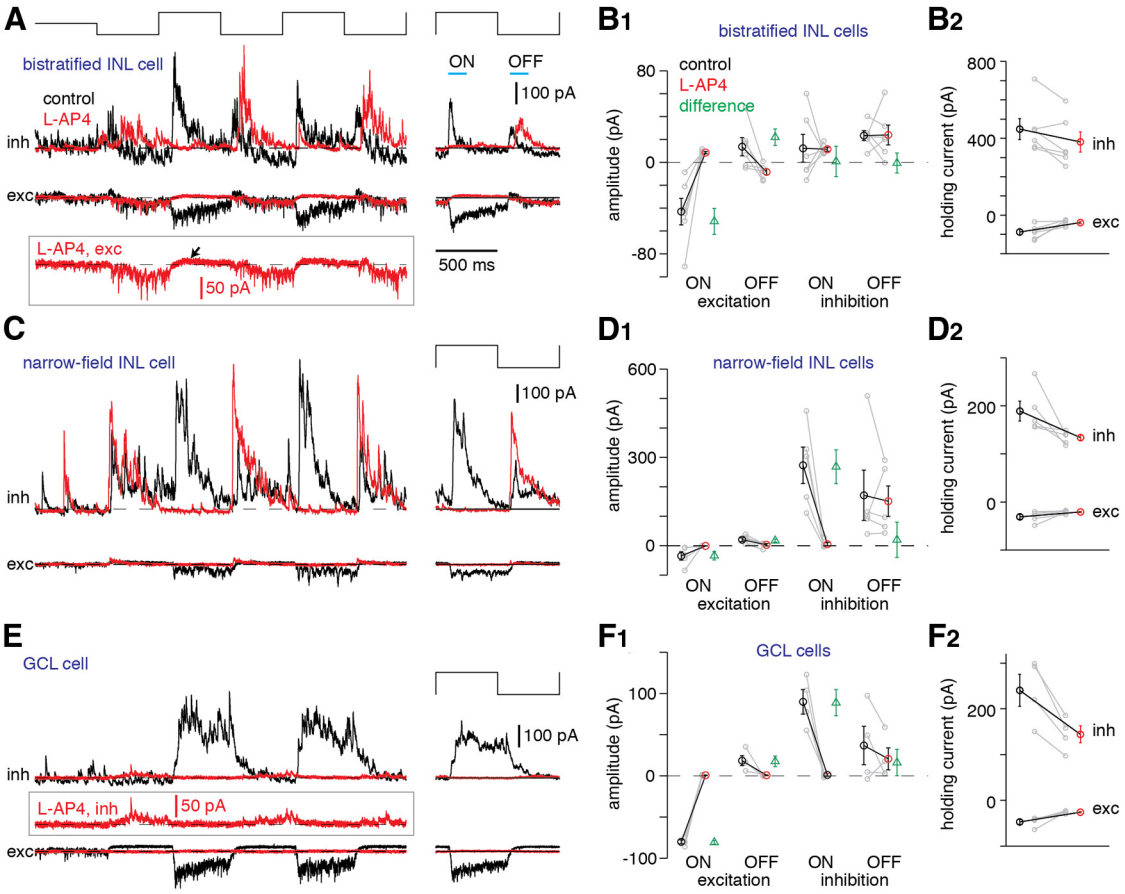

Figure 5. Convergence of ON and OFF bipolar cell inputs to VIP$^+$ cells. ***A***, Left, Voltage-clamp recordings of excitatory current (exc; V_{hold} near inhibitory reversal, −67 mV) and inhibitory current (inh; V_{hold} near excitatory reversal, 0 mV) in a bistratified INL cell in response to a 1 Hz contrast-reversing spot (300 μm diameter, 100% contrast). Red traces represent the same measurements in the presence of L-AP4 (20 μM) to block the ON pathway. Excitatory current measured in the presence of L-AP4 is shown a second time for clarity, with an expanded scale (twice the originally plotted amplitude; inset in ***A***). Light offset caused a sluggish inward current, consistent with OFF bipolar cell input; whereas light onset caused a small, sustained outward current accompanied by reduced synaptic noise (arrow), consistent with the suppression of basal excitatory input. Traces have been baseline-subtracted (baseline indicated by horizontal dashed line). Right, Average cycle of excitatory and inhibitory current, combined across two repeats at each of two holding potentials bracketing the appropriate reversal potential (see Materials and Methods). ON and OFF time windows indicate periods where current was averaged for population analysis (see ***B$_1$***). ***B$_1$***, Excitatory and inhibitory input in the ON and OFF time windows in ***A*** under control (black) and drug (red) conditions. Measurements from individual cells are shown in gray. Green points indicate the difference between control and drug conditions. Error bars indicate ±1 SEM across cells. Across cells, spot diameter was either 200 or 300 μm. ***B$_2$***, The holding current during measurements of excitatory and inhibitory current. Error bars indicate ±1 SEM across cells. ***C***, ***D***, Same format as ***A*** and ***B***, but for narrow-field INL cells. ***E***, ***F***, Same format as ***A*** and ***B***, but for GCL cells. For the example cell (***E***), the inhibitory current measured in the presence of L-AP4 is shown a second time for clarity, with an expanded scale (twice the originally plotted amplitude; inset).

function with L-AP4 (20 μM) (Slaughter and Miller, 1981). In bistratified INL cells ($n = 6$), L-AP4 blocked excitatory input at light onset (by 51 ± 11 pA; $t = 4.56$; $p < 0.01$) but had variable effects on inhibitory input at light onset (Fig. 5*A*,*B$_1$*). The presence of this apparent (albeit small-amplitude) inhibition in the presence of L-AP4 likely reflects the difficulty with voltage-clamping bistratified INL cells, related to the electrical coupling described above. Notably, L-AP4 also revealed sluggish excitatory input at light offset (Fig. 5*A*, inset, *B$_1$*). In the presence of L-AP4, tonic excitation was suppressed at light onset, resulting in an outward current accompanied by reduced synaptic noise.

In narrow-field INL cells ($n = 5$), L-AP4 blocked both excitatory (by 34 ± 14 pA; $t = 2.36$; $p < 0.05$) and inhibitory inputs (by 268 ± 57 pA; $t = 4.67$; $p < 0.01$) at light onset but did not significantly affect inhibitory input at light offset (Fig. 5*C*,*D$_1$*). In GCL cells ($n = 4$), L-AP4 likewise blocked both excitatory (by 80 ± 2 pA; mean ± SEM; $t = 35.6$; $p < 0.001$) and inhibitory inputs (by 89 ± 16 pA; $t = 5.57$; $p < 0.01$) at light onset (Fig. 5*E*,*F$_1$*). This condition isolated inhibitory input onto GCL cells at light offset, which was relatively small in most cells (Figure 5*E*, inset, *F$_1$*).

L-AP4 changed the holding current in some cases. While recording inhibition, the holding current for bistratified INL cells and GCL cells was reduced by 67 ± 26 pA ($t = 2.59$; $p < 0.05$) and 96 ± 18 pA ($t = 5.20$; $p < 0.01$), respectively; the narrow-field INL cells showed the same trend (55 ± 22 pA change; $t = 2.55$; $p < 0.10$). The holding current while recording excitation in bistratified INL cells and GCL cells became more positive in the presence of L-AP4 by 49 ± 15 pA ($t = 3.24$; $p < 0.05$) and 21 ± 6 pA ($t = 3.49$; $p < 0.05$), respectively; the narrow-field INL cells showed the same trend (more positive by 10.1 ± 4.4 pA; $p < 0.10$). Blocking the ON bipolar cell pathway apparently reduced basal inhibitory and excitatory inputs onto VIP$^+$ cells.

Spatial receptive field properties of synaptic inputs to three VIP$^+$ cell types

To characterize the spatial properties of synaptic inputs onto VIP$^+$ cells, we measured synaptic currents while varying the diameter of a contrast-reversing spot stimulus. For all three cell types, excitatory input at light onset peaked for spot diameters <300 μm (Fig. 6*A*). The spatial tuning for each cell type

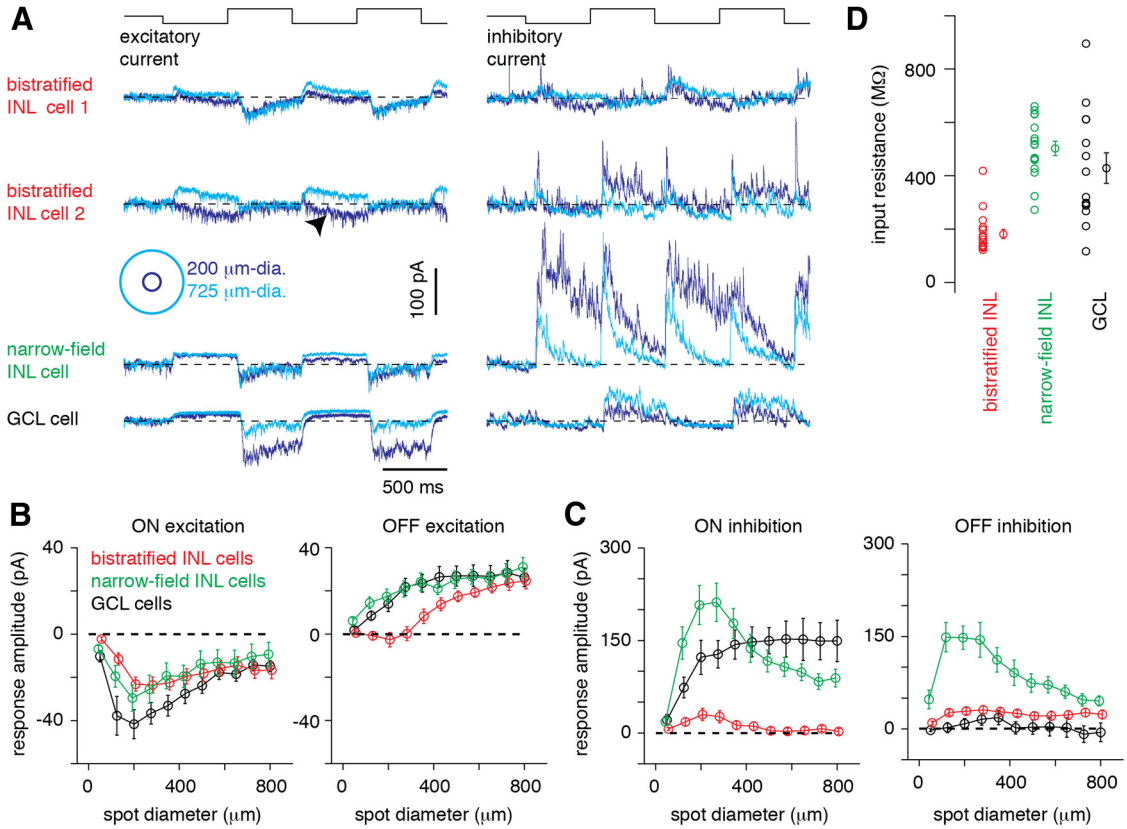

Figure 6. Spatial tuning of synaptic inputs to VIP$^+$ cells. ***A***, VIP$^+$ cell synaptic current responses to a 1 Hz contrast-reversing spot (100% contrast) of either 200 (dark blue) or 725 μm diameter (light blue). Traces have been baseline-subtracted (baseline, horizontal dashed line). Excitatory current was recorded near the reversal potential for inhibition, and vice versa. Panel represents two examples of bistratified INL cells with varying degrees of excitatory input at light offset. Bistratified INL cell 2 showed an obvious inward current at light offset for the small spot stimulus (arrowhead). ***B***, Spatial tuning of excitatory current during the ON and OFF phases of the stimulus. Responses represent the average current within a 150 ms time window starting from the peak of the response amplitude, following light onset or offset (averaged over three cycles). Error bars indicate $\pm$1 SEM across cells. ***C***, Same format as ***B*** for the inhibitory current amplitude during ON and OFF phases of the stimulus, as a function of spot size. ***D***, Input resistance for each of the three VIP$^+$ cell types. Individual data for each type are shown next to the mean $\pm$ SEM across cells.

was apparent in the population plot of response-versus-spot diameter (Fig. 6*B*). To determine whether the tuning was consistent across cells, we quantified the difference between the average excitatory input evoked by small spots (200 and 275 μm diameter) versus large spots (725 and 800 μm diameter). Excitatory input evoked by small spots was significantly larger than the input evoked by large spots for bistratified INL cells ($n = 18$; difference of 6.7 $\pm$ 2.6 pA; $t = 2.56$; $p < 0.02$), narrow-field INL cells ($n = 17$; difference of 18 $\pm$ 4 pA; $t = 4.61$; $p < 0.001$), and GCL cells ($n = 14$; difference of 25 $\pm$ 5 pA; mean $\pm$ SEM; $t = 4.86$; $p < 0.001$). At light offset, the narrow-field INL and GCL cells showed outward currents, consistent with suppression of basal excitatory input that increased with spot diameter (Fig. 6*B*); the same was true for bistratified INL cells for large spot stimuli. For small spots, bistratified INL cell excitatory input at light offset was, on average, near zero; but this reflected the variability across the sample. In some cells, the excitatory input at light offset was relatively small, with an initial outward current (i.e., suppressed baseline excitatory input) followed by a slow return to baseline (Fig. 6*A*; bistratified INL cell 1); whereas in other cells, there was a clear excitatory inward current at light offset (Fig. 6*A*; bistratified INL cell 2). The variability in this excitatory response to small, dark spots seemed to reflect integration of inputs from ON bipolar cells (i.e., sustained outward current) and OFF bipolar cells (i.e., sluggish inward current, with variable amplitude across cells).

Inhibitory input was generally weak in bistratified INL cells (Fig. 6*C*) but did show spatial tuning for the response at light onset, as reflected by larger inhibitory inputs evoked by small spots relative to large spots (difference of 25 $\pm$ 5 pA; $t = 5.46$; $p < 0.002$). By contrast, inhibitory input was relatively large in narrow-field INL and GCL cells (Fig. 6*C*). For narrow-field INL cells, inhibitory input peaked for small spots, relative to large spots, for responses at both light onset (difference of 124 $\pm$ 20 pA; $t = 6.22$; $p < 0.001$) and offset (difference of 100 $\pm$ 18 pA; $t = 5.51$; $p < 0.001$). For GCL cells, inhibitory input at light onset increased with spot size (Fig. 6*C*).

In the course of voltage-clamp measurements, we noted differences in input resistance (R_{in}; see Materials and Methods) between the cell types (Fig. 6*D*). R_{in} of the bistratified INL cells (181 $\pm$ 17 MΩ; $n = 18$) was less than R_{in} of both narrow-field INL cells (503 $\pm$ 27 MΩ; mean $\pm$ SEM; $n = 17$; $t = 10.1$; $p < 0.001$) and GCL cells (429 $\pm$ 57 MΩ; $n = 14$; $t = 4.14$; $p < 0.001$). The difference in R_{in} between narrow-field and bistratified INL cells may be used for determining the cell type before imaging the dendritic tree. The above R_{in} measurements were made using the Cs-based pipette solution, which could block certain resting conductances and overestimate the cell's normal input resistance. However, similar results were observed in a smaller sample of cells recorded with K-based pipette solution: R_{in} of the bistratified INL cells (207 $\pm$ 26 MΩ; $n = 14$, one outlier removed) was less than R_{in} of both narrow-field INL cells (426 $\pm$ 49 MΩ; mean $\pm$ SEM; $n = 8$; $t =$

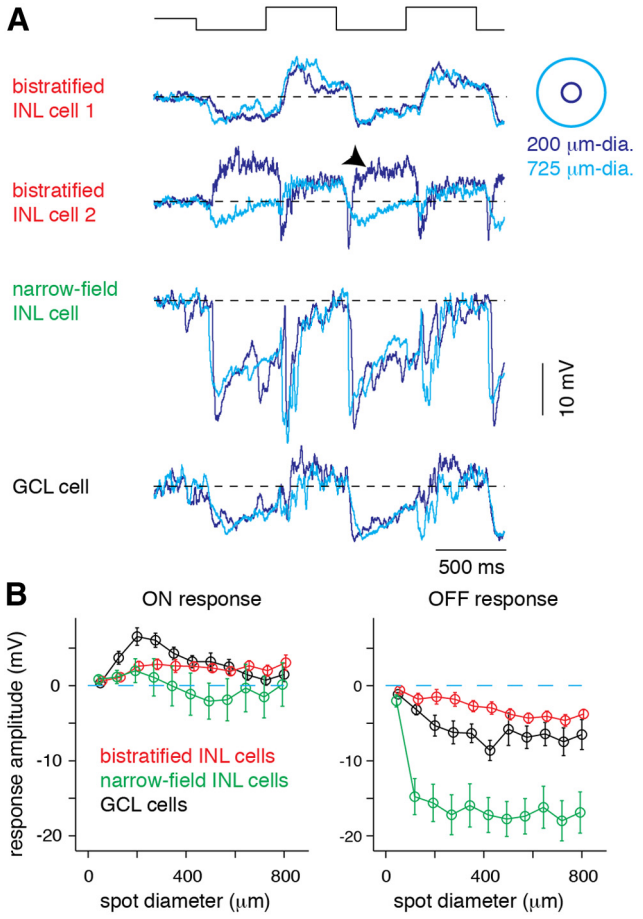

Figure 7. Spatial tuning of voltage responses in VIP+ cells. ***A***, VIP+ cell membrane voltage responses to a 1 Hz contrast-reversing spot (100% contrast) of either 200 (dark blue) or 725 μm diameter (light blue). Traces have been baseline-subtracted (resting potential, horizontal dashed line). Panel represents two examples of bistratified INL cells with varying degrees of depolarization during light offset. Bistratified INL cell 2 depolarized at light offset for the small spot stimulus (arrowhead). ***B***, Spatial tuning of membrane potential responses during the ON and OFF phases of the stimulus. Responses represent the average membrane potential within a 150 ms time window starting from the peak of the response amplitude, following light onset or offset (averaged over three cycles). Error bars indicate ±1 SEM across cells.

2.78; $p < 0.01$) and GCL cells (394 ± 53 MΩ; $n = 7$; $t = 2.18$; $p < 0.03$). The high R_{in} of narrow-field INL cells predicts that the large inhibitory currents described above (Fig. 5) strongly influence the membrane potential of this cell type.

Spatial receptive fields of three VIP+ cell types measured in membrane potential responses

To understand how the pattern of synaptic input influenced the membrane potential of the VIP+ cells, we studied voltage responses with current-clamp recordings (Fig. 7*A*). Spatial tuning (Fig. 7*B*) was quantified, as above, by comparing the average responses to small spots (200 and 275 μm diameter) versus large spots (725 and 800 μm diameter). Voltage responses at light onset (ON) and offset (OFF) were measured as changes from each cell types' resting potential, which measured −47.8 ± 1.5 mV (mean ± SEM; $n = 15$) in bistratified INL cells, −44.6 ± 3.3 mV ($n = 8$) in narrow-field INL cells, and −53.5 ± 3.4 mV ($n = 7$) in GCL cells.

For bistratified INL cells ($n = 15$), the depolarization at light onset was relatively small and untuned (Fig. 7*B*). For narrow-field INL cells ($n = 8$), the spot response was not significantly tuned (difference between small and large spots, 2.2 ± 1.2 mV; $t = 1.74$; $p < 0.07$). In these cells, the response at light onset was commonly biphasic, showing a transient hyperpolarization superimposed on a sustained depolarization (Fig. 7*A*). For GCL cells ($n = 7$), the depolarization at light onset was tuned to small spots (difference between small and large spots, 5.2 ± 1.1 mV; $t = 4.92$; $p < 0.002$).

For all cell types, the average response at light offset was a hyperpolarization that increased with spot diameter (Fig. 7*B*). We compared the amplitude of this hyperpolarization (averaged over the two largest spot sizes) between cell types. Narrow-field INL cells showed larger hyperpolarizations than both bistratified INL cells ($t = 5.76$; $p < 0.001$) and GCL cells ($t = 4.08$; $p < 0.002$), and GCL cells showed significantly larger hyperpolarizations than bistratified cells ($t = 2.09$; $p < 0.05$). Thus, hyperpolarization amplitude distinguished the function of the three VIP+ cell types, with strikingly large hyperpolarizations in narrow-field INL cells. In the extreme cases, individual narrow-field INL cells hyperpolarized 25 mV negative to their ~−45 mV resting potential.

Approximately half of the bistratified INL cells showed a depolarizing response at both light onset and offset (7 of 15 cells; Fig. 7*A*). The variability in the response at light offset reflected a similar variability observed in the excitatory currents for this cell type (Fig. 6*A*) and may ultimately be explained by the variable structure of the dendritic tree across cells.

Optogenetic responses of VIP+ cells

We next aimed to assess VIP+ cell connections with identified ganglion cells, using optogenetics. The retina presents a unique challenge for optogenetic experiments because the native photoreceptors are inherently light sensitive. We determined conditions necessary to suppress the photoreceptor input to bipolar cells while presenting the extremely bright ChR2-activating stimulus used below (peak, 450 nm; intensity, 5.3×10^{17} Q s^{-1} cm^{-2}; 0.22 × 0.22 mm^2) (Beier et al., 2013). Initially, we bath-applied the AMPA/kainate receptor antagonist (DNQX, 100 μM) to block the photoreceptor→OFF bipolar cell synapses and L-AP4 (20 μM) to block the photoreceptor→ON bipolar cell synapses; an NMDA receptor antagonist was also applied (D-AP4, 100 μM). We monitored bipolar cell glutamate release in the IPL of a wild-type retina with two-photon imaging of the biosensor iGluSnFR, expressed on both ganglion and amacrine cell processes (Fig. 8*A*; see Materials and Methods) (Borghuis et al., 2013, 2014). Although DNQX and L-AP4 together blocked photoreceptor-mediated bipolar cell release to a conventional light stimulus in an earlier study (Borghuis et al., 2014), the extremely bright ChR2 stimulus generated a persistent iGluSnFR signal in an OFF layer centered at 70% IPL depth (re GCL, 0%; INL, 100%). This response was completely suppressed after adding the selective kainate receptor antagonist UBP310 (50 μM) (Buldyrev et al., 2012), which blocks the glutamate input to OFF bipolar cell dendrites (Borghuis et al., 2014). The residual activity in the absence of UBP310 apparently reflected competitive interaction of DNQX and synaptic glutamate following the photoreceptors' high rate of release at light offset. The following experiments used the combined drug mixture (DNQX, L-AP4, D-AP5, UBP310) to silence photoreceptor-mediated bipolar cell release in response to ChR2 stimulation.

To determine the range of ChR2 stimulus strengths that gives natural-like (physiological) levels of depolarization, we first measured ChR2-mediated responses in VIP+ amacrine cells in the

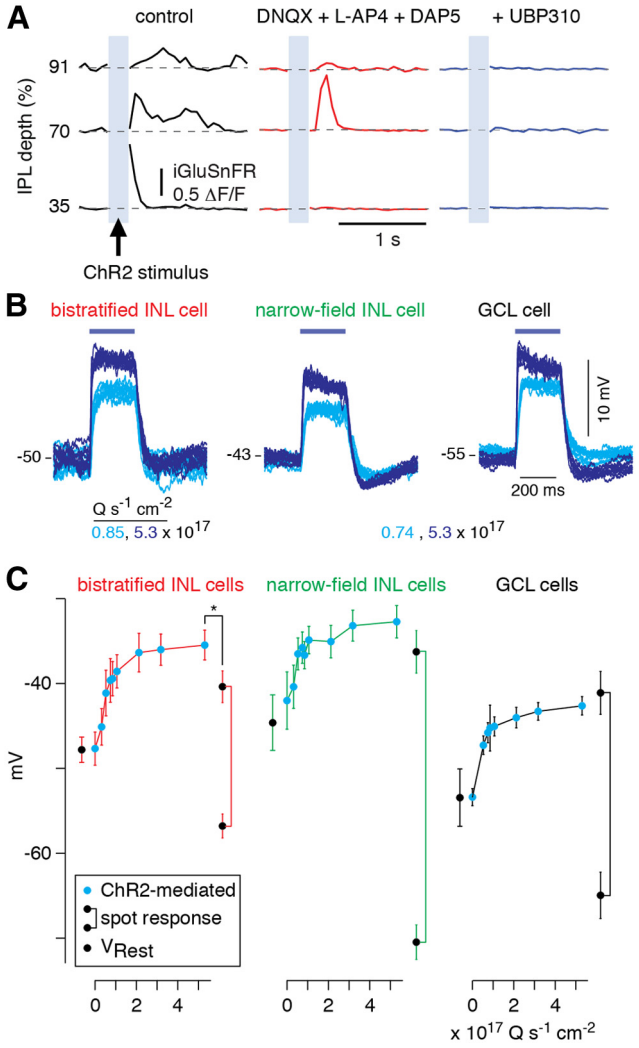

Figure 8. ChR2-mediated responses in VIP$^+$ cells. ***A***, Two-photon fluorescence recordings of iGluSnFR responses at multiple levels within the IPL (relative to GCL, 0% and INL, 100%). Each trace represents the fluorescence response to the ChR2 stimulus; a response to light onset is observed in an inner layer (35%; partly overlapping with stimulus presentation) and responses following light offset are observed in outer layers (70, 91%). Responses in control conditions are mostly blocked by DNQX (100 μM), L-AP4 (20 μM), and D-AP5 (100 μM), but transient OFF responses persisted at the 70% layer. These residual responses were eliminated by additional block with UBP310 (50 μM). ***B***, Example responses (12 repeats) to ChR2 stimulation in a bistratified INL cell (light vs dark blue: 0.85 vs 5.3×10^{17} Q s^{-1} cm^{-2}), a narrow-field INL, and a GCL cell (light vs dark blue: 0.74 vs 5.3×10^{17} Q s^{-1} cm^{-2}). Responses were recorded in the presence of the blockers used in ***A*** (DNQX, L-AP4, D-AP5, UBP310). ***C***, Population responses to various levels of ChR2 stimulation recorded in synaptic blockers, in each of three cell types (cyan points). Responses were averaged over a 200 ms time window during the sustained portion of the ChR2 response (20–220 ms after stimulus onset). For each cell type, the resting membrane potential in control medium (i.e., no synaptic blockers) is shown to the left of the resting potential in synaptic blockers (i.e., cyan point at 0×10^{17} Q s^{-1} cm^{-2}). The range of membrane depolarization and hyperpolarization in response to spot stimuli (from Fig. 7) is shown, with a connected line, to the right of the maximal ChR2 response; these data represent the maximum and minimum voltage measured across all spot sizes at the sampling rate (i.e., not averaged within a time window). Error bars indicate ± 1 SEM across cells. In the case of bistratified INL cells, depolarization to maximum ChR2 stimulus exceeded the maximum depolarization to spot stimuli. *$p < 0.001$.

VIP-ires-Cre::Ai32 mouse (see Materials and Methods). In the presence of the drug mixture, we recorded VIP$^+$ cells in whole-cell current-clamp configuration while stimulating with increasing levels of ChR2 stimulation (Fig. 8*B*). In the presence of the blockers, the GCL cells rested at −53.4 ± 1.0 mV (mean ± SEM; $n = 4$), which was significantly more negative than narrow-field INL cells (−42.0 ± 3.4 mV; $n = 4$) and bistratified INL cells (−47.7 ± 1.9 mV; $n = 6$). For each cell type, the resting potential was similar to the resting potential measured in the absence of the drugs (see above; $p > 0.10$ for each comparison; Fig. 8*C*). In all cases, ChR2 stimulation caused a sustained membrane depolarization that increased with stimulation intensity (range, 0–5.3×10^{17} Q s^{-1} cm^{-2}). In response to the brightest intensity, the maximum depolarization from rest was similar, and not significantly different between the three cell types: bistratified INL cells (12.2 ± 0.5 mV), narrow-field INL cells (9.3 ± 1.6 mV), and GCL cells (10.8 ± 1.4 mV; $p > 0.10$ for each comparison) (Fig. 8*C*).

We compared the ChR2-mediated responses of each cell type to the average resting potential and membrane depolarization in response to contrast stimulation (Fig. 8*C*). We measured the maximum depolarization from rest, in each cell type, in response to each cell's optimal spot size. These measurements of maximum depolarization were obtained from raw traces and therefore exceeded the depolarization averaged over the time window used in the population analysis above (Fig. 7*B*). Maximum depolarization from rest in the bistratified INL cell was 7.4 ± 0.6 mV, which was significantly less than the maximum depolarization (12.2 ± 0.5 mV) in the ChR2 experiment ($t = 6.17$; $p < 0.001$). Peak depolarizations from rest in the narrow-field INL and GCL cells were 8.4 ± 1.3 mV and 12.4 ± 1.3 mV, respectively, which were not different from the maximum depolarizations in the ChR2 experiment for each cell type ($p > 0.10$ for each case).

We conclude that the maximum depolarization to the ChR2 stimulus evokes a response as large or larger than the maximum depolarization to a contrast-reversing spot. Thus, the ChR2 stimulus is sufficient to drive VIP$^+$ cells through their physiological ranges. For bistratified INL cells, the ChR2 stimulation apparently exceeded the maximum depolarization to spot stimulation. This discrepancy may reflect primarily the site of synaptic excitation in the two experiments. Spot stimulation evoked synaptic release onto the dendrites and caused a local depolarization that would be attenuated at the soma, whereas the ChR2 stimulation opened depolarizing channels across the entire cell, including the soma.

Functional connections between VIP$^+$ cells and specific ganglion cell types

To study the synaptic outputs of VIP$^+$ amacrine cells onto ganglion cells, we recorded from identified ganglion cell types in the VIP-ires-Cre::Ai32 mouse while stimulating ChR2 in the presence of the synaptic blockers (L-AP4, DNQX, D-AP5, UBP310). This combination blocks most of the glutamate receptors in the retina (mGluR6, AMPA, kainate, NMDA) but leaves GABAergic synaptic transmission intact. OFF δ cells were targeted based on their large soma size and identified by their OFF-sustained light response (before pharmacological block) (Borghuis et al., 2014). In addition, cell identity was confirmed after recording, based on dendrite stratification near the INL, assessed by two-photon imaging (Margolis and Detwiler, 2007; Borghuis et al., 2014). In the presence of the blockers, ChR2 stimulation evoked inhibitory currents superimposed on spontaneous inhibitory activity. The response to maximal ChR2 stimulation (5.3×10^{17} Q s^{-1} cm^{-2}) was significant (221 ± 72 pA; mean ± SEM; $n = 9$; $t = 3.05$; $p < 0.01$) but notably variable across cells (Fig. 9*F*). The most sensitive cells, on the other hand, responded even during weak ChR2 stimulation (Fig. 9*A*, *G*).

Strong ChR2-evoked responses were found also in ON-OFF DS cells (Fig. 9*B*) and in W3 cells (Fig. 9*C*). ON-OFF DS cells were

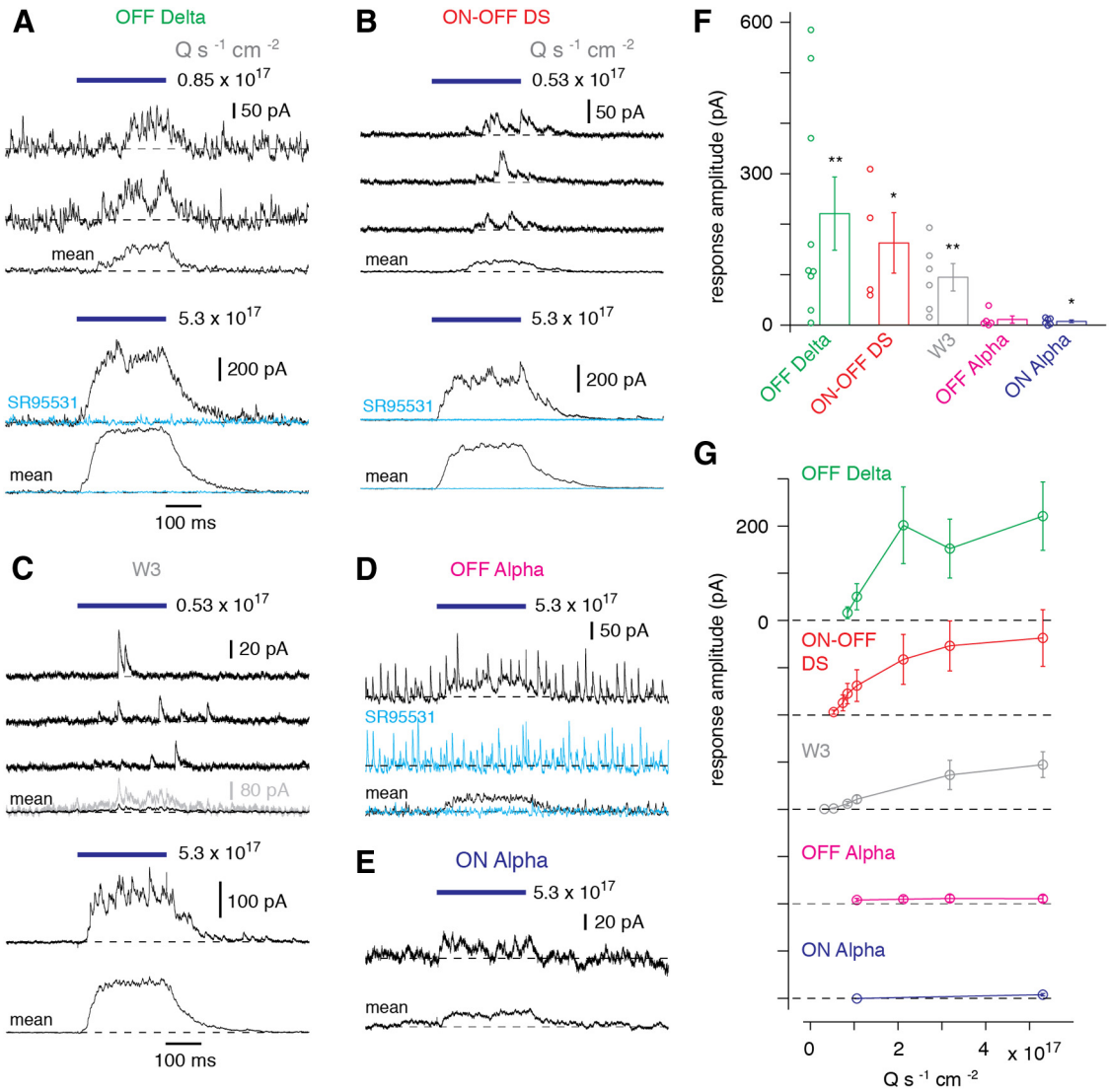

Figure 9. Optogenetic studies of VIP+ cell connections to five ganglion cell types. ***A***, Inhibitory currents recorded in an OFF δ ganglion cell in the VIP-ires-Cre::Ai32 retina during ChR2 stimulation of VIP+ cells. Individual trials show a high level of synaptic noise at baseline accompanied by responses at two levels of ChR2 stimulation. Mean traces (bottom) represent the average across 12 repeats. The response to maximal ChR2 stimulation was blocked by the GABA-A receptor antagonist SR95531 (50 μM). Dashed line in each case indicates the baseline current before ChR2 stimulation. All recordings were performed in the presence of the blockers described in Figure 8 (DNQX, L-AP4, D-AP5, UBP310). ***B***, Same format as ***A*** for an ON-OFF DS ganglion cell. Here, spontaneous inhibitory activity is minimal, and weak ChR2 stimulation evoked apparent summation of several individual synaptic events. The strong ChR2-mediated response was blocked by SR95531. ***C***, Same format as ***A*** for a W3 ganglion cell labeled in a VIP-ires-Cre::Ai32::TYW3 retina. As in ***B***, there is minimal spontaneous inhibitory activity at baseline and individual events can be resolved during weak ChR2 stimulation. For clarity, the mean inhibitory current to weak stimulation is plotted a second time with an expanded vertical scale (gray). ***D***, OFF α ganglion cell response to strong ChR2 stimulation. A small inhibitory current was observed that was blocked by SR95531. SR95531 did not block the spontaneous inhibitory input, suggesting that its origin was glycinergic. ***E***, Same format as ***D*** for an ON α cell. A small ChR2-mediated inhibitory current is observed to maximal ChR2 stimulation. ***F***, Average inhibitory current to maximal ChR2 stimulation (5.3×10^{17} Q s^{-1} cm^{-2}) for each ganglion cell type. Individual cells are shown (circles) next to the population mean. Error bars indicate ±1 SEM across cells. Significant responses are indicated as follows: *$p < 0.05$. **$p < 0.01$. ***G***, Average inhibitory current to varying levels of ChR2 stimulation in each cell type. Error bars indicate ±1 SEM across cells ($n = 3$ or more cells per point).

identified in VIP-ires-Cre::Ai32 mice by testing for direction selectivity of ganglion cells with medium-sized somas using methods described previously (Park et al., 2014). W3 cells were targeted in triple transgenic VIP-ires-Cre::Ai32::TYW3 mice, by targeting brightly fluorescent cells in the ganglion cell layer (Zhang et al., 2012) (see Materials and Methods). For both ON-OFF DS and W3 ganglion cells, there was very little spontaneous inhibitory activity in the presence of the synaptic blockers. In response to weak ChR2 stimulation, both ON-OFF DS and W3 cells showed apparent quantal responses distributed randomly in time during the ChR2 stimulation. The strongest stimulus evoked a step-like outward current apparently reflecting the release of multiple, overlapping vesicles. These maximal responses were significant for both ON-OFF DS cells (163 ± 60 pA; $n = 4$; $t = 2.7$; $p < 0.05$) and W3 cells (95 ± 27 pA; $n = 6$; $t = 3.48$; $p < 0.01$).

Finally, we recorded both ON and OFF α cells in the VIP-ires-Cre::Ai32 mouse by targeting large somas (Fig. 9*D*,*E*). Cell types were confirmed by transient ON and OFF light responses, respectively, and by the dendrite stratification level, as described previously (Margolis and Detwiler, 2007; Borghuis et al., 2013, 2014). In the presence of the blockers, OFF α cells showed primarily weak responses that were inconsistent across cells. The OFF α cell with the largest ChR2 response, evoked by the brightest light level tested, is shown in Figure 9*D*. ON α cells also showed relatively weak responses (Fig. 9*E*). On average, re-

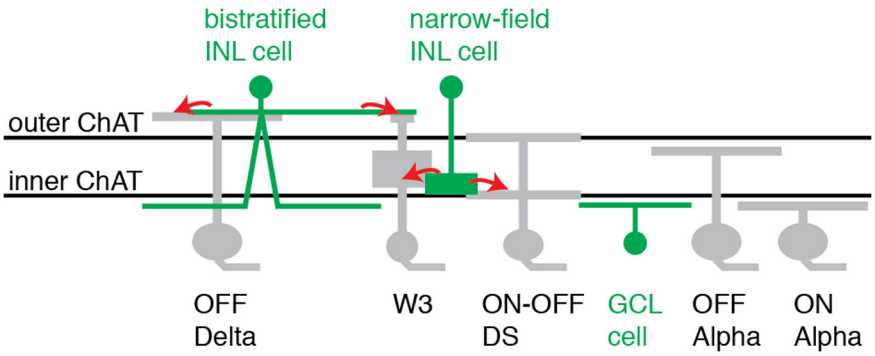

Figure 10. Circuit diagrams for VIP$^+$ cells. Proposed synaptic output of the three major VIP$^+$ cell types. Bistratified INL cells are positioned near the INL, where they make synapses with OFF δ ganglion cells and W3 cells. Narrow-field INL cells make inhibitory synapses with both W3 and ON-OFF DS cells near the inner ChAT band. GCL cells are positioned near the ON α ganglion cell dendrites but apparently do not provide substantial synaptic output to either the ON α or any of the other ganglion cell types shown here.

sponses to the brightest level of ChR2 stimulation showed a trend toward significance for OFF α cells (11 ± 7 pA; $n = 5$; $t = 1.55$; $p < 0.10$) and reached significance for ON α cells (7.5 ± 2.6 pA; $n = 6$; $t = 2.83$; $p < 0.02$). However, in both cases, response size was negligible compared with the typical light-evoked inhibitory current in these cells, which can exceed 500 pA (Pang et al., 2003; Murphy and Rieke, 2006; Ke et al., 2014).

In summary, ChR2-evoked responses were detected in all five recorded ganglion cell types. Three of these types (OFF δ, ON-OFF DS, W3) showed strong and consistent responses that increased with stimulation level over a ~5-fold range (Fig. 9*G*). ChR2-mediated responses were blocked by the GABA-A receptor antagonist SR95531 ($n = 5$; one ON-OFF DS, one OFF α, three OFF δ; Fig. 9*A*,*B*,*D*). We conclude that VIP$^+$ cells make functional GABAergic synapses strongly with some of the recorded cell types (OFF δ, ON-OFF DS, W3) and weakly and inconsistently with others (ON, OFF α).

Discussion

Retinal amacrine cells play fundamental roles in visual processing, but most of the ~30–40 types have been barely characterized, due to the difficulty in targeting individual cell types for routine study of their function and synaptic connections. With the aid of transgenic mice, one can now target and manipulate specific amacrine cell types (Beier et al., 2013; Zhu et al., 2014). Here, we used a transgenic mouse line in which VIP$^+$ interneurons express Cre recombinase. The labeling of VIP$^+$ cells in our study differed from the pattern reported previously (Zhu et al., 2014). The previous study used a combination of AAV and rabies virus to induce sparse, but intense fluorescence in Cre-expressing cells and identified the bistratified INL cell. Our study, using either targeted dye filling or AAV methods, identified two additional types (Fig. 2): monostratified cells with somas in the GCL (GCL cells) and narrow-field monostratified cells with somas in the INL (narrow-field INL cells). GCL cell density was highest in the dorsal retina (Fig. 1), suggesting either that GCL cells show regional differences in density or that their somas are displaced to the INL in the ventral retina.

The synaptic inputs and receptive field properties of VIP$^+$ cell types were diverse, suggesting that each VIP cell type plays a unique role in visual processing. The bistratified INL cell receives excitatory input from both ON and OFF bipolar cell pathways (Fig. 5). Excitation at light offset is relatively sluggish (Fig. 5*A*,B_1), possibly mediated by the costratifying Type 1/2 OFF bipolar cell types (Wässle et al., 2009). Furthermore, the bistratified INL cell integrates inhibition mediated by both ON and OFF bipolar cell pathways. The bistratified INL cell also receives input through gap junctions with coupled cells, which apparently include neighboring cells of the same type (Figs. 3, 4). The narrow-field INL cell receives excitation mediated by ON bipolar cells along with strong inhibition mediated by both ON and OFF bipolar pathways. Finally, the GCL cell receives both excitatory and inhibitory inputs mediated by ON bipolar cells (Figs. 3, 5). Notably, GCL cells showed the most prominent spatial tuning in their membrane potential (Fig. 7), driven by spatially tuned excitatory input and untuned inhibitory input (Fig. 6).

Functional connections of VIP$^+$ cells were studied using optogenetics (Figs. 8, 9). ChR2-mediated depolarizations from rest were similar in each VIP$^+$ cell type, ~9–12 mV (Fig. 8*B*,*C*). ChR2-mediated inhibitory responses in postsynaptic OFF δ, ON-OFF DS, and W3 ganglion cells were strong, whereas responses in ON and OFF α cells were weak and inconsistent (Fig. 9). The dendritic stratification of each cell type under study suggests the following preliminary connectivity diagram (Fig. 10). OFF δ cells receive input from bistratified INL cells because both stratify near the INL. W3 cells receive input from both bistratified INL and narrow-field INL cells because their dendrites ramify broadly (Kim et al., 2010; Zhang et al., 2012). ON-OFF DS cells receive input from narrow-field INL cells because both cell types stratify near the inner ChAT band. ON α cells showed weak ChR2-mediated input, suggesting that they do not make substantial contact with the costratifying GCL cells. Thus, the primary synaptic targets of the GCL cells are apparently types of ganglion cell other than those studied here, as well as bipolar cell axon terminals. The latter connection would have gone undetected in our optogenetic paradigm because we blocked the glutamate receptor channels (AMPA and NMDA) necessary for studying bipolar cell synapses. Likewise, connections to other amacrine cells were not explored but may be a primary postsynaptic target of some VIP$^+$ cells, as found in ultrastructural studies of guinea pig retina (Lee et al., 2002). VIP$^+$ interneurons in visual cortex also commonly contact other interneurons (Pfeffer et al., 2013; Pi et al., 2013; Fu et al., 2014).

Role of inhibition in bipolar cell synaptic release onto VIP$^+$ cells

Our experiments blocking GABA-A and glycine receptors revealed a role for these channels in regulating glutamate release onto VIP$^+$ cells. Apparently, the initial mode of sustained release by the presynaptic bipolar terminals onto both narrow-field INL and GCL cells required intact inhibition within the circuit (Fig. 3*C*,*E*) (Borghuis et al., 2014). If the blockers reduced inhibition of presynaptic bipolar terminals, these terminals might have experienced an unusually large depolarization resulting in transient release followed by vesicle depletion, which could explain the transient postsynaptic response (Singer and Diamond, 2003). The apparent oscillations in the excitatory currents might be explained by altered amacrine cell feedback onto the presynaptic bipolar terminals, which could be mediated by intact GABA-C receptors under our conditions (Arai et al., 2004). Previously, we

found that blocking all feedback pathways (with DNQX) caused sustained glutamate release to become transient, as measured by iGluSnFR imaging (Borghuis et al., 2014). Collectively, these results suggest that sustained glutamate release from certain bipolar cell types requires intact inhibition.

Possible roles of VIP cells in retinal circuit function

Bistratified INL cells might form a circuit for "cross-over" inhibition between the ON and OFF pathways (Demb and Singer, 2012). For example, these cells were commonly depolarized in response to large, bright stimuli (Fig. 7), which could cause them to release GABA at light onset onto OFF δ cells. Indeed, OFF δ (OFF-sustained) cells receive a mixture of glycinergic and GABAergic inhibition at light onset (Murphy and Rieke, 2006; Di Marco et al., 2013). Presently, we cannot determine what fraction of the GABAergic input to an OFF δ cell is mediated by VIP$^+$ cells. However, we note that the OFF δ cell's ~200 pA inhibitory current evoked by ChR2 stimulation of VIP cells (Fig. 9) is a substantial fraction of the 780 ± 220 pA (mean ± SEM) inhibitory current response amplitude that we measured in response to a contrast-modulating spot stimulus ($n = 5$ cells; data not shown). However, understanding the precise contribution of VIP$^+$ cells to the light response requires further study.

The complex dendritic tree of bistratified INL cells raises the possibility of independent signaling in subcellular compartments (Grimes et al., 2010). However, presumed ON bipolar cell synaptic input to the inner dendrites (near the GCL) was detectable by recording from the soma, demonstrating that ON bipolar cell-mediated signals do not remain strictly local (Figs. 3–7). Whether or not bistratified INL cells exhibit local, independent processing within the dendritic tree may be addressed using calcium imaging (Euler et al., 2002; Grimes et al., 2010; Borghuis et al., 2011). The bistratified INL cell differs from other ON-OFF amacrine cell types, which are more transient and can fire action potentials (Taylor, 1996; Völgyi et al., 2001; Davenport et al., 2007; Pang et al., 2010; Knop et al., 2011, 2014; Greschner et al., 2014).

Narrow-field INL cells showed pronounced hyperpolarization to light offset (Fig. 7), mediated by strong inhibition and suppressed excitation (Figs. 5, 6). The combination of these two influences generated untuned hyperpolarization for spot sizes >0.1 mm (Fig. 7*B*). The observed hyperpolarization is well suited for a disinhibition mechanism (i.e., reducing a tonic level of inhibition at light offset in postsynaptic cells). Such disinhibition may be paired with increased excitation to enhance the contrast response in the postsynaptic cell (Manookin et al., 2008; Manu and Baccus, 2011; Chen and Li, 2012; Sher and DeVries, 2012). This model presumes that the narrow-field INL cells tonically release GABA at rest. However, our ChR2 experiments suggested that some cells that are activated by VIP$^+$ cell stimulation, including ON-OFF DS and W3 ganglion cells, receive little tonic inhibitory input, at least in the presence of synaptic blockers (Fig. 9*B*,*C*). Presently, it is unclear whether or not VIP$^+$ cells, including narrow-field INL cells, release GABA tonically at rest in the intact circuit.

GCL cells showed the simplest receptive fields: spatially tuned ON responses (Figs. 3, 5–7). These cells are poised to generate an inhibitory subunit that could be integrated with excitatory ON bipolar cell subunits to shape ganglion cell firing (Münch et al., 2009; Borghuis et al., 2013). Understanding further the role of VIP$^+$ cells in visual processing awaits complementary strategies for cell inactivation or ablation (Nirenberg and Meister, 1997; Vlasits et al., 2014).

References

Applebury ML, Antoch MP, Baxter LC, Chun LL, Falk JD, Farhangfar F, Kage K, Krzystolik MG, Lyass LA, Robbins JT (2000) The murine cone photoreceptor: a single cone type expresses both S and M opsins with retinal spatial patterning. Neuron 27:513–523. CrossRef Medline

Arai I, Yamada Y, Asaka T, Tachibana M (2004) Light-evoked oscillatory discharges in retinal ganglion cells are generated by rhythmic synaptic inputs. J Neurophysiol 92:715–725. CrossRef Medline

Badea TC, Nathans J (2004) Quantitative analysis of neuronal morphologies in the mouse retina visualized by using a genetically directed reporter. J Comp Neurol 480:331–351. CrossRef Medline

Baden T, Schubert T, Chang L, Wei T, Zaichuk M, Wissinger B, Euler T (2013) A tale of two retinal domains: near-optimal sampling of achromatic contrasts in natural scenes through asymmetric photoreceptor distribution. Neuron 80:1206–1217. CrossRef Medline

Beier KT, Borghuis BG, El-Danaf RN, Huberman AD, Demb JB, Cepko CL (2013) Transsynaptic tracing with vesicular stomatitis virus reveals novel retinal circuitry. J Neurosci 33:35–51. CrossRef Medline

Borghuis BG, Tian L, Xu Y, Nikonov SS, Vardi N, Zemelman BV, Looger LL (2011) Imaging light responses of targeted neuron populations in the rodent retina. J Neurosci 31:2855–2867. CrossRef Medline

Borghuis BG, Marvin JS, Looger LL, Demb JB (2013) Two-photon imaging of nonlinear glutamate release dynamics at bipolar cell synapses in the mouse retina. J Neurosci 33:10972–10985. CrossRef Medline

Borghuis BG, Looger LL, Tomita S, Demb JB (2014) Kainate receptors mediate signaling in both transient and sustained OFF bipolar cell pathways in mouse retina. J Neurosci 34:6128–6139. CrossRef Medline

Buldyrev I, Puthussery T, Taylor WR (2012) Synaptic pathways that shape the excitatory drive in an OFF retinal ganglion cell. J Neurophysiol 107:1795–1807. CrossRef Medline

Caldwell JH, Daw NW (1978) New properties of rabbit retinal ganglion cells. J Physiol 276:257–276. CrossRef Medline

Caldwell JH, Daw NW, Wyatt HJ (1978) Effects of picrotoxin and strychnine on rabbit retinal ganglion cells: lateral interactions for cells with more complex receptive fields. J Physiol 276:277–298. CrossRef Medline

Casini G, Brecha NC (1992) Colocalization of vasoactive intestinal polypeptide and GABA immunoreactivities in a population of wide-field amacrine cells in the rabbit retina. Vis Neurosci 8:373–378. CrossRef Medline

Chen S, Li W (2012) A color-coding amacrine cell may provide a blue-off signal in a mammalian retina. Nat Neurosci 15:954–956. CrossRef Medline

Cohen E, Sterling P (1990) Demonstration of cell types among cone bipolar neurons of cat retina. Philos Trans R Soc Lond B Biol Sci 330:305–321. CrossRef Medline

Davenport CM, Detwiler PB, Dacey DM (2007) Functional polarity of dendrites and axons of primate A1 amacrine cells. Vis Neurosci 24:449–457. CrossRef Medline

Demb JB, Singer JH (2012) Intrinsic properties and functional circuitry of the AII amacrine cell. Vis Neurosci 29:51–60. CrossRef Medline

Di Marco S, Protti DA, Solomon SG (2013) Excitatory and inhibitory contributions to receptive fields of alpha-like retinal ganglion cells in mouse. J Neurophysiol 110:1426–1440. CrossRef Medline

Dunn FA, Wong RO (2014) Wiring patterns in the mouse retina: collecting evidence across the connectome, physiology and light microscopy. J Physiol 592:4809–4823. CrossRef Medline

Estevez ME, Fogerson PM, Ilardi MC, Borghuis BG, Chan E, Weng S, Auferkorte ON, Demb JB, Berson DM (2012) Form and function of the M4 cell, an intrinsically photosensitive retinal ganglion cell type contributing to geniculocortical vision. J Neurosci 32:13608–13620. CrossRef Medline

Euler T, Detwiler PB, Denk W (2002) Directionally selective calcium signals in dendrites of starburst amacrine cells. Nature 418:845–852. CrossRef Medline

Euler T, Haverkamp S, Schubert T, Baden T (2014) Retinal bipolar cells: elementary building blocks of vision. Nat Rev Neurosci 15:507–519. CrossRef Medline

Farrow K, Teixeira M, Szikra T, Viney TJ, Balint K, Yonehara K, Roska B (2013) Ambient illumination toggles a neuronal circuit switch in the retina and visual perception at cone threshold. Neuron 78:325–338. CrossRef Medline

Fu Y, Tucciarone JM, Espinosa JS, Sheng N, Darcy DP, Nicoll RA, Huang ZJ, Stryker MP (2014) A cortical circuit for gain control by behavioral state. Cell 156:1139–1152. CrossRef Medline

Greschner M, Field GD, Li PH, Schiff ML, Gauthier JL, Ahn D, Sher A, Litke AM, Chichilnisky EJ (2014) A polyaxonal amacrine cell population in the primate retina. J Neurosci 34:3597–3606. CrossRef Medline

Grimes WN, Zhang J, Graydon CW, Kachar B, Diamond JS (2010) Retinal parallel processors: more than 100 independent microcircuits operate within a single interneuron. Neuron 65:873–885. CrossRef Medline

Gustincich S, Feigenspan A, Wu DK, Koopman LJ, Raviola E (1997) Control of dopamine release in the retina: a transgenic approach to neural networks. Neuron 18:723–736. CrossRef Medline

Helmstaedter M, Briggman KL, Turaga SC, Jain V, Seung HS, Denk W (2013) Connectomic reconstruction of the inner plexiform layer in the mouse retina. Nature 500:168–174. CrossRef Medline

Hommel JD, Sears RM, Georgescu D, Simmons DL, DiLeone RJ (2003) Local gene knockdown in the brain using viral-mediated RNA interference. Nat Med 9:1539–1544. CrossRef Medline

Jackson CR, Ruan GX, Aseem F, Abey J, Gamble K, Stanwood G, Palmiter RD, Iuvone PM, McMahon DG (2012) Retinal dopamine mediates multiple dimensions of light-adapted vision. J Neurosci 32:9359–9368. CrossRef Medline

Jadzinsky PD, Baccus SA (2013) Transformation of visual signals by inhibitory interneurons in retinal circuits. Annu Rev Neurosci 36:403–428. CrossRef Medline

Jakobs TC, Ben Y, Masland RH (2003) CD15 immunoreactive amacrine cells in the mouse retina. J Comp Neurol 465:361–371. CrossRef Medline

Ke JB, Wang YV, Borghuis BG, Cembrowski MS, Riecke H, Kath WL, Demb JB, Singer JH (2014) Adaptation to background light enables contrast coding at rod bipolar cell synapses. Neuron 81:388–401. CrossRef Medline

Kim IJ, Zhang Y, Meister M, Sanes JR (2010) Laminar restriction of retinal ganglion cell dendrites and axons: subtype-specific developmental patterns revealed with transgenic markers. J Neurosci 30:1452–1462. CrossRef Medline

Knop GC, Feigenspan A, Weiler R, Dedek K (2011) Inputs underlying the ON-OFF light responses of type 2 wide-field amacrine cells in TH::GFP mice. J Neurosci 31:4780–4791. CrossRef Medline

Knop GC, Pottek M, Monyer H, Weiler R, Dedek K (2014) Morphological and physiological properties of enhanced green fluorescent protein (EGFP)-expressing wide-field amacrine cells in the ChAT-EGFP mouse line. Eur J Neurosci 39:800–810. CrossRef Medline

Kolb H (1979) The inner plexiform layer in the retina of the cat: electron microscopic observations. J Neurocytol 8:295–329. CrossRef Medline

Kolb H, Nelson R (1983) Rod pathways in the retina of the cat. Vision Res 23:301–312. CrossRef Medline

Kolb H, Nelson R, Mariani A (1981) Amacrine cells, bipolar cells and ganglion cells of the cat retina: a Golgi study. Vision Res 21:1081–1114. CrossRef Medline

Lee EJ, Shon WH, Kim IB, Kwon SO, Oh SJ, Chun MH (2002) Localization of CD15 immunoreactivity in the rat retina. Cell Tissue Res 310:131–136. CrossRef Medline

Lee S, Zhou ZJ (2006) The synaptic mechanism of direction selectivity in distal processes of starburst amacrine cells. Neuron 51:787–799. CrossRef Medline

Lee S, Chen L, Chen M, Ye M, Seal RP, Zhou ZJ (2014) An unconventional glutamatergic circuit in the retina formed by vGluT3 amacrine cells. Neuron 84:708–715. CrossRef Medline

Lin B, Masland RH (2006) Populations of wide-field amacrine cells in the mouse retina. J Comp Neurol 499:797–809. CrossRef Medline

Lorén I, Tornqvist K, Alumets J (1980) VIP (vasoactive intestinal polypeptide)-immunoreactive neurons in the retina of the rat. Cell Tissue Res 210:167–170. Medline

MacNeil MA, Masland RH (1998) Extreme diversity among amacrine cells: implications for function. Neuron 20:971–982. CrossRef Medline

MacNeil MA, Heussy JK, Dacheux RF, Raviola E, Masland RH (1999) The shapes and numbers of amacrine cells: matching of photofilled with Golgi-stained cells in the rabbit retina and comparison with other mammalian species. J Comp Neurol 413:305–326. CrossRef Medline

Madisen L, Zwingman TA, Sunkin SM, Oh SW, Zariwala HA, Gu H, Ng LL, Palmiter RD, Hawrylycz MJ, Jones AR, Lein ES, Zeng H (2010) A robust and high-throughput Cre reporting and characterization system for the whole mouse brain. Nat Neurosci 13:133–140. CrossRef Medline

Madisen L, Mao T, Koch H, Zhuo JM, Berenyi A, Fujisawa S, Hsu YW, Garcia AJ 3rd, Gu X, Zanella S, Kidney J, Gu H, Mao Y, Hooks BM, Boyden ES, Buzsáki G, Ramirez JM, Jones AR, Svoboda K, Han X, et al. (2012) A toolbox of Cre-dependent optogenetic transgenic mice for light-induced activation and silencing. Nat Neurosci 15:793–802. CrossRef Medline

Manookin MB, Beaudoin DL, Ernst ZR, Flagel LJ, Demb JB (2008) Disinhibition combines with excitation to extend the operating range of the OFF visual pathway in daylight. J Neurosci 28:4136–4150. CrossRef Medline

Manu M, Baccus SA (2011) Disinhibitory gating of retinal output by transmission from an amacrine cell. Proc Natl Acad Sci U S A 108:18447–18452. CrossRef Medline

Margolis DJ, Detwiler PB (2007) Different mechanisms generate maintained activity in ON and OFF retinal ganglion cells. J Neurosci 27:5994–6005. CrossRef Medline

Marvin JS, Borghuis BG, Tian L, Cichon J, Harnett MT, Akerboom J, Gordus A, Renninger SL, Chen TW, Bargmann CI, Orger MB, Schreiter ER, Demb JB, Gan WB, Hires SA, Looger LL (2013) An optimized fluorescent probe for visualizing glutamate neurotransmission. Nat Methods 10:162–170. CrossRef Medline

Masland RH (2012a) The neuronal organization of the retina. Neuron 76:266–280. CrossRef Medline

Masland RH (2012b) The tasks of amacrine cells. Vis Neurosci 29:3–9. CrossRef Medline

McMahon DG, Iuvone PM, Tosini G (2014) Circadian organization of the mammalian retina: from gene regulation to physiology and diseases. Prog Retin Eye Res 39:58–76. CrossRef Medline

Münch TA, da Silveira RA, Siegert S, Viney TJ, Awatramani GB, Roska B (2009) Approach sensitivity in the retina processed by a multifunctional neural circuit. Nat Neurosci 12:1308–1316. CrossRef Medline

Murphy GJ, Rieke F (2006) Network variability limits stimulus-evoked spike timing precision in retinal ganglion cells. Neuron 52:511–524. CrossRef Medline

Newkirk GS, Hoon M, Wong RO, Detwiler PB (2013) Inhibitory inputs tune the light response properties of dopaminergic amacrine cells in mouse retina. J Neurophysiol 110:536–552. CrossRef Medline

Nikonov SS, Kholodenko R, Lem J, Pugh EN Jr (2006) Physiological features of the S- and M-cone photoreceptors of wild-type mice from single-cell recordings. J Gen Physiol 127:359–374. CrossRef Medline

Nirenberg S, Meister M (1997) The light response of retinal ganglion cells is truncated by a displaced amacrine circuit. Neuron 18:637–650. CrossRef Medline

Pan F, Mills SL, Massey SC (2007) Screening gap junction antagonists on dye coupling in the rabbit retina. Vis Neurosci 24:609–618. CrossRef Medline

Pang JJ, Gao F, Wu SM (2003) Light-evoked excitatory and inhibitory synaptic inputs to ON and OFF alpha ganglion cells in the mouse retina. J Neurosci 23:6063–6073. Medline

Pang JJ, Abd-El-Barr MM, Gao F, Bramblett DE, Paul DL, Wu SM (2007) Relative contributions of rod and cone bipolar cell inputs to AII amacrine cell light responses in the mouse retina. J Physiol 580:397–410. CrossRef Medline

Pang JJ, Gao F, Wu SM (2010) Light responses and morphology of bNOS-immunoreactive neurons in the mouse retina. J Comp Neurol 518:2456–2474. CrossRef Medline

Pang JJ, Gao F, Wu SM (2012) Physiological characterization and functional heterogeneity of narrow-field mammalian amacrine cells. J Physiol 590:223–234. CrossRef Medline

Park SJ, Kim IJ, Looger LL, Demb JB, Borghuis BG (2014) Excitatory synaptic inputs to mouse on-off direction-selective retinal ganglion cells lack direction tuning. J Neurosci 34:3976–3981. CrossRef Medline

Peichl L, González-Soriano J (1994) Morphological types of horizontal cell in rodent retinae: a comparison of rat, mouse, gerbil, and guinea pig. Vis Neurosci 11:501–517. CrossRef Medline

Pfeffer CK, Xue M, He M, Huang ZJ, Scanziani M (2013) Inhibition of inhibition in visual cortex: the logic of connections between molecularly distinct interneurons. Nat Neurosci 16:1068–1076. CrossRef Medline

Pi HJ, Hangya B, Kvitsiani D, Sanders JI, Huang ZJ, Kepecs A (2013) Cortical interneurons that specialize in disinhibitory control. Nature 503:521–524. CrossRef Medline

Pologruto TA, Sabatini BL, Svoboda K (2003) ScanImage: flexible software for operating laser scanning microscopes. Biomed Eng Online 2:13. CrossRef Medline

Roska B, Werblin F (2001) Vertical interactions across ten parallel, stacked

representations in the mammalian retina. Nature 410:583–587. CrossRef Medline

Sagar SM (1987) Somatostatin-like immunoreactive material in the rabbit retina: immunohistochemical staining using monoclonal antibodies. J Comp Neurol 266:291–299. CrossRef Medline

Seung HS, Sümbül U (2014) Neuronal cell types and connectivity: lessons from the retina. Neuron 83:1262–1272. CrossRef Medline

Sher A, DeVries SH (2012) A non-canonical pathway for mammalian blue-green color vision. Nat Neurosci 15:952–953. CrossRef Medline

Singer JH, Diamond JS (2003) Sustained Ca^{2+} entry elicits transient postsynaptic currents at a retinal ribbon synapse. J Neurosci 23:10923–10933. Medline

Slaughter MM, Miller RF (1981) 2-Amino-4-phosphonobutyric acid: a new pharmacological tool for retina research. Science 211:182–185. CrossRef Medline

Sümbül U, Zlateski A, Vishwanathan A, Masland RH, Seung HS (2014) Automated computation of arbor densities: a step toward identifying neuronal cell types. Front Neuroanat 8:139. CrossRef Medline

Taniguchi H, He M, Wu P, Kim S, Paik R, Sugino K, Kvitsiani D, Fu Y, Lu J, Lin Y, Miyoshi G, Shima Y, Fishell G, Nelson SB, Huang ZJ (2011) A resource of Cre driver lines for genetic targeting of GABAergic neurons in cerebral cortex. Neuron 71:995–1013. CrossRef Medline

Taylor WR (1996) Response properties of long-range axon-bearing amacrine cells in the dark-adapted rabbit retina. Vis Neurosci 13:599–604. CrossRef Medline

Thoreson WB, Mangel SC (2012) Lateral interactions in the outer retina. Prog Retin Eye Res 31:407–441. CrossRef Medline

Tikidji-Hamburyan A, Reinhard K, Seitter H, Hovhannisyan A, Procyk CA, Allen AE, Schenk M, Lucas RJ, Münch TA (2015) Retinal output changes qualitatively with every change in ambient illuminance. Nat Neurosci 18:66–74. CrossRef Medline

Tornqvist K, Uddman R, Sundler F, Ehinger B (1982) Somatostatin and VIP neurons in the retina of different species. Histochemistry 76:137–152. CrossRef Medline

Vaney DI, Sivyer B, Taylor WR (2012) Direction selectivity in the retina: symmetry and asymmetry in structure and function. Nat Rev Neurosci 13:194–208. CrossRef Medline

Veruki ML, Hartveit E (2009) Meclofenamic acid blocks electrical synapses of retinal AII amacrine and on-cone bipolar cells. J Neurophysiol 101:2339–2347. CrossRef Medline

Vlasits AL, Bos R, Morrie RD, Fortuny C, Flannery JG, Feller MB, Rivlin-Etzion M (2014) Visual stimulation switches the polarity of excitatory input to starburst amacrine cells. Neuron 83:1172–1184. CrossRef Medline

Völgyi B, Xin D, Amarillo Y, Bloomfield SA (2001) Morphology and physiology of the polyaxonal amacrine cells in the rabbit retina. J Comp Neurol 440:109–125. CrossRef Medline

Wang YV, Weick M, Demb JB (2011) Spectral and temporal sensitivity of cone-mediated responses in mouse retinal ganglion cells. J Neurosci 31:7670–7681. CrossRef Medline

Wässle H, Puller C, Müller F, Haverkamp S (2009) Cone contacts, mosaics, and territories of bipolar cells in the mouse retina. J Neurosci 29:106–117. CrossRef Medline

Wei W, Hamby AM, Zhou K, Feller MB (2011) Development of asymmetric inhibition underlying direction selectivity in the retina. Nature 469:402–406. CrossRef Medline

Werblin FS (2010) Six different roles for crossover inhibition in the retina: correcting the nonlinearities of synaptic transmission. Vis Neurosci 27:1–8. CrossRef Medline

Zhang C, McCall MA (2012) Receptor targets of amacrine cells. Vis Neurosci 29:11–29. CrossRef Medline

Zhang Y, Kim IJ, Sanes JR, Meister M (2012) The most numerous ganglion cell type of the mouse retina is a selective feature detector. Proc Natl Acad Sci U S A 109:E2391-E2398. CrossRef Medline

Zhu Y, Xu J, Hauswirth WW, DeVries SH (2014) Genetically targeted binary labeling of retinal neurons. J Neurosci 34:7845–7861. CrossRef Medline